

TRANS: Terrain-aware Reinforcement Learning for Agile Navigation of Quadruped Robots under Social Interactions

Wei Zhu¹, Irfan Tito Kurniawan¹, Ye Zhao², and Mistuhiro Hayashibe¹

Abstract—This study introduces TRANS: Terrain-aware Reinforcement learning for Agile Navigation under Social interactions, a deep reinforcement learning (DRL) framework for quadrupedal social navigation over unstructured terrains. Conventional quadrupedal navigation typically separates motion planning from locomotion control, neglecting whole-body constraints and terrain awareness. On the other hand, end-to-end methods are more integrated but require high-frequency sensing, which is often noisy and computationally costly. In addition, most existing approaches assume static environments, limiting their use in human-populated settings. To address these limitations, we propose a two-stage training framework with three DRL pipelines. (1) TRANS-Loco employs an asymmetric actor-critic (AC) model for quadrupedal locomotion, enabling traversal of uneven terrains without explicit terrain or contact observations. (2) TRANS-Nav applies a symmetric AC framework for social navigation, directly mapping transformed LiDAR data to ego-agent actions under differential-drive kinematics. (3) A unified pipeline, TRANS, integrates TRANS-Loco and TRANS-Nav, supporting terrain-aware quadrupedal navigation in uneven and socially interactive environments. Comprehensive benchmarks against locomotion and social navigation baselines demonstrate the effectiveness of TRANS. Hardware experiments further confirm its potential for sim-to-real transfer.

Index Terms—Reinforcement learning, social navigation, quadrupedal locomotion, sim-to-real transfer

I. INTRODUCTION

QUADRUPED robots exhibit superior maneuverability compared to their wheeled counterparts, allowing them to navigate uneven terrain and execute dynamic maneuvers in complex environments. While locomotion on irregular surfaces has been extensively studied [1], navigation challenges, such as collision avoidance and target reaching in uneven and dynamic environments, remain comparatively underexplored (see Fig. 1). Such capabilities are essential for deploying agile robots in socially interactive and real-world settings. Existing navigation frameworks [2] often decouple motion planning from locomotion control, which tends to neglect critical whole-body constraints. Conversely, while end-to-end frameworks [3] attempt to unify these layers, they generally demand high-frequency exteroceptive sensing that is often precluded by onboard computational constraints and inherent sensor noise.

Compared to quadrupedal platforms, the navigation of wheeled mobile robots in static environments is well-established [4]–[7], encompassing both map-based planners

¹The authors are with the Department of Robotics, Graduate School of Engineering, Tohoku University, 980-8579, Sendai, Japan. zhu.wei.c1@tohoku.ac.jp

²The author is with the Laboratory for Intelligent Decision and Autonomous Robots, Woodruff School of Mechanical Engineering, Georgia Institute of Technology, Atlanta, GA 30313, USA. yezhao@gatech.edu

Project website: <https://tohoku-neurobotics.github.io/trance.github.io/>. Code will be open-sourced soon.

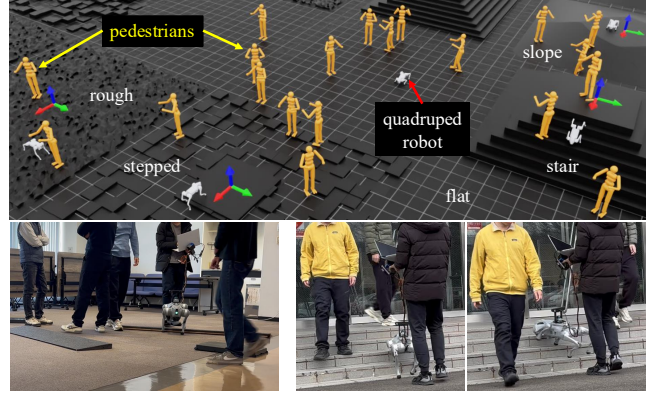


Fig. 1. Terrain-aware navigation of quadruped robots in socially interactive environments. The top panel illustrates simulation training scenarios, while the bottom panels show real-world implementations.

and end-to-end pipelines. While the non-evolving nature of static scenes facilitates real-world deployment, navigation in dynamic environments remains a formidable challenge due to complex, implicit agent interactions, such as human–human and human–robot coordination. Current model-based approaches generally assume constant pedestrian velocities and overlook these latent social interactions [8]. Furthermore, while predictive models can forecast pedestrian trajectories by taking interactions into consideration [9], their practical utility is often hampered by out-of-distribution (OOD) data and robot–model mismatch. Although end-to-end pipelines offer a potential solution [10], they typically rely on high-fidelity expert demonstrations or assume omnidirectional kinematics that neglect physical constraints. Moreover, methods reliant on raw sensor observations [11] often face significant sim-to-real gaps due to geometric and perceptual discrepancies between simulated and real-world entities.

In this work, we propose TRANS: Terrain-aware Reinforcement learning for Agile Navigation under Social interactions. Our approach decouples quadrupedal locomotion from social navigation by independently training two distinct DRL policies. We first utilize an asymmetric actor–critic (AC) architecture that operates without explicit terrain maps or contact states. Concurrently, a symmetric AC framework is developed for social navigation, employing a differential-drive model governed by kinematic constraints. Subsequently, the social navigation policy is fine-tuned and extended for the quadrupedal platform, yielding a unified, hierarchical policy capable of robust quadrupedal navigation in uneven and human-populated environments.

The primary contributions of this study are as follows:

- **Terrain-aware quadrupedal locomotion.** We develop an agile quadrupedal locomotion controller that operates without explicit terrain maps or contact state estimation through an asymmetric AC architecture, thereby streamlining hardware deployment.
- **Social navigation with transformed LiDAR scans.** We present a navigation policy that implicitly captures socially interactive features from transformed LiDAR scans. This approach streamlines the sim-to-real transfer without relying on fully known environments, significantly facilitating real-world implementations.
- **Unified navigation and locomotion.** We propose an integrated architecture that harmonizes high-level motion planning with low-level locomotion. This unification allows for the optimization of navigation paths while maintaining strict adherence to the robot's whole-body constraints and terrain awareness.
- **Comprehensive benchmarks and hardware evaluations.** We reproduce and extend state-of-the-art (SOTA) benchmarks for quadrupedal locomotion and conduct rigorous comparative analyses against both traditional model-based planners and DRL-based baselines. Finally, we demonstrate the practical efficacy of our framework through successful sim-to-real deployment on a physical quadruped platform.

The remainder of this article is organized as follows. Section II provides a review of relevant literature. Section III introduces the proposed framework and formalizes the problem. Section IV details the locomotion controller, and Section V presents the social navigation policy. In Section VI, we describe the integrated algorithm for quadrupedal navigation in socially interactive, uneven environments. The performance of the locomotion, navigation, and unified frameworks is evaluated through simulation in Sections VII, VIII, and IX, respectively. Section X discusses the technical details of the sim-to-real transfer and hardware deployment. Finally, Section XI addresses the limitations of the current study, and Section XII concludes the paper.

II. RELATED WORK

This section provides a comprehensive review of the relevant literature. We first review navigation strategies for wheeled mobile robots, given their widespread deployment in socially interactive environments. These strategies are categorized into two primary paradigms: classical model-based approaches and learning-based pipelines. Subsequently, we summarize the state of the research regarding quadrupedal locomotion, focusing specifically on the integration of these controllers into navigation frameworks.

A. Model-based Navigation Approaches

Model-based navigation for mobile robots in dynamic environments relies on explicit environmental representations, robot dynamics, and predicted agent trajectories to generate control actions. For instance, given the robot's kinematics (e.g., differential-drive models) and the state information of surrounding agents, such as geometry, position, and velocity,

the Dynamic Window Approach (DWA) [12], [13] executes a discrete search over the feasible action space. However, DWA typically assumes constant pedestrian velocities within a fixed planning horizon, which often results in unnatural maneuvers or collision failures when encountering interactive, time-varying pedestrian behaviors.

Assuming fully observable agent states, the Social Force Model (SFM) [14], [15] and Optimal Reciprocal Collision Avoidance (ORCA) [16], [17] optimize the trajectories of interacting agents through local force or velocity-space constraints. However, SFM lacks explicit collision avoidance guarantees, while ORCA assumes reciprocity—a condition where all agents share equal responsibility for collision avoidance. Although variants such as Variable Responsibility ORCA (VR-ORCA) [18] and AdaptiVe Optimal Collision Avoidance Driven by Opinion (AVOCADO) [19] relax this assumption, these methods remain inherently reactive. By prioritizing immediate state-based actions over long-horizon trajectory planning, they are prone to oscillations and unnatural detours in dense or symmetric configurations. Additionally, their heavy reliance on precise agent geometry and kinematic data necessitates highly accurate sensing, which is often difficult to maintain in real-world scenarios.

To facilitate long-horizon planning and mitigate unnatural behaviors in symmetric interactions, Model Predictive Control (MPC)-based frameworks have gained significant traction for navigation in dynamic environments. For example, Safe Horizon MPC (SH-MPC) [20] explicitly constrains collision probabilities throughout the planned trajectory, while Topology-driven MPC (T-MPC) [21] integrates global guidance as a topological constraint for local motion planning. Despite these advancements, both approaches often assume constant pedestrian velocities over the planning horizon, which limits their adaptability to complex social interactions.

To address this limitation, the Neural Proximal Alternating-minimization Network (NeuPAN) [22] utilizes a Deep Unfolded Neural Encoder (DUNE) to predict collision points directly from raw LiDAR point clouds, which are then used to inform the MPC planner. Beyond raw point cloud data, the Stochastic Cartographic Occupancy Prediction Engine (SCOPE) [23] utilizes a Variational Autoencoder (VAE) to predict potential collision regions from occupancy grid maps (OGMs). Similarly, spatiotemporal OGMs have been employed for dynamic scene prediction via self-supervised learning frameworks [24]. However, such predictive models are trained on specific datasets, potentially compromising their generalization to novel environments or unseen pedestrian behaviors. Moreover, MPC-based navigation often exhibits over-conservative behavior, particularly when navigating socially interactive environments where feasible paths are narrow.

B. End-to-end Navigation Pipelines

In contrast to model-based approaches, end-to-end navigation pipelines offer a more streamlined architecture by bypassing the explicit integration of perception and planning, eliminating the need for online optimization, and reducing the burden of manual parameter tuning. Collision Avoidance with

Deep Reinforcement Learning (CADRL) [25] pioneered this paradigm by directly mapping agent observations to control actions. However, CADRL primarily accounts for pairwise interactions between the robot and individual agents, neglecting the broader collective dynamics of the socially interactive scenarios. Subsequent frameworks, such as Self-Attention RL (SARL) [26] and Relational Graph Learning (RGL) [27], address this by leveraging attention mechanisms and Graph Neural Networks (GNNs) to model implicit multi-agent interactions. Despite these advancements, such methods often assume perfect state estimation, including agent geometry and preferred velocities, which exacerbates the sim-to-real gap due to their heavy reliance on high-fidelity perception. Moreover, these pipelines frequently require expert demonstrations for pre-training and typically assume omnidirectional kinematics. This lack of consideration for physical motion constraints limits their applicability to complex robotic platforms with non-holonomic or strict kinematic limitations.

An alternative, more direct paradigm utilizes DRL to map raw sensor observations into control actions. For instance, Hybrid-RL [11] incorporates an RL policy alongside two specialized safety and efficiency modules tailored for hazardous and low-complexity scenarios, respectively. In standard environments, the RL agent directly transforms continuous LiDAR scans into velocity commands for a differential-drive robot. While this hierarchical approach offers a balance of safety and performance, the robust classification of scenarios remains a significant challenge. Consequently, recent research has shifted toward developing unified DRL policies capable of generalizing across diverse environments. Social Policy [28] extracts latent interaction features from sequential LiDAR data, while Learning to Navigate in Dynamic environments with Normalized LiDAR scans (LNDNL) [29] leverages Long Short-Term Memory (LSTM) networks to capture spatiotemporal dynamics. Similarly, Distilling Privileged information for Crowd-Aware Navigation (DiPCAN) [30] maps depth imagery to robot actions by distilling privileged pedestrian state information. Beyond raw scans, intermediate representations such as occupancy maps [31] and risk maps [32] are frequently employed to encode social geometry. However, high-dimensional image processing entails significant computational overhead, and map-based abstractions often suffer from degraded spatial resolution in expansive environments. Furthermore, the use of continuous LiDAR scans inherently couples ego-motion with pedestrian dynamics, potentially hindering learning efficiency and the asymptotic performance of the policy.

Integrating raw sensor data with privileged pedestrian states, such as precise positions and velocities, enables the extraction of richer interaction features [33]–[35]. However, the practical utility of these methods is often limited by the need for sophisticated perception and estimation pipelines to provide such ground-truth information in real-time. In addition to DRL, Imitation Learning (IL) [36]–[39] and Inverse Reinforcement Learning (IRL) [40]–[42] have gained traction for social navigation, capitalizing on the increasing availability of human-trajectory datasets. Despite their ability to mimic social norms, these data-driven approaches are frequently constrained by their training distributions; they often exhibit poor general-

ization or failure when encountering out-of-distribution (OOD) scenarios that deviate from the expert demonstrations.

C. Quadrupedal Locomotion

Traversing uneven terrain typically necessitates the generation of elevation maps [43]–[46] to represent the topography beneath and surrounding the quadruped robot. However, maintaining high-frequency updates for these maps is often precluded by limited onboard computational resources. Moreover, map quality is frequently compromised by noise and motion blur resulting from oscillatory locomotion dynamics. To develop locomotion policies independent of explicit elevation maps, the teacher-student paradigm with a two-stage learning framework [47]–[51] has emerged as a prominent solution. Furthermore, two-stage learning frameworks are employed to modulate foot placement atop foundational gaits, such as those governed by Central Pattern Generators (CPGs) [52].

Rather than employing a two-stage training pipeline, single-stage asymmetric actor–critic (AC) techniques have become a cornerstone of sim-to-real RL. A notable example is Dream Walking for Quadrupedal robots (DreamWaQ) [53], where the critic is augmented with privileged information during training, while the actor operates exclusively on proprioceptive states to ensure feasible hardware deployment. Conversely, some approaches dispense with privileged information entirely by adopting symmetric AC learning, as seen in Self-learning Latent Representation (SLR) [54]. In this work, we extend the DreamWaQ architecture for our locomotion module. By leveraging asymmetric observations, we eliminate the need for explicit exteroceptive perception, thereby facilitating a direct and efficient sim-to-real transfer.

D. Quadrupedal Navigation

Despite the maturity of wheeled mobile robot navigation, legged navigation particularly in dynamic settings, remains an open challenge due to the intricacies of high-dimensional robot dynamics and irregular terrain. Prevailing methodologies generally decouple legged navigation into a two-tier hierarchy [2], [55]–[63]: a high-level planner generates a feasible Center-of-Mass (CoM) trajectory, which a low-level whole-body controller (WBC) is then tasked to track. However, these hierarchical frameworks often struggle to maintain consistency between the planning and execution layers, as they fail to fully incorporate low-level locomotion constraints and the geometric nuances of uneven terrain when planning the CoM trajectory.

End-to-end quadrupedal navigation pipelines [3], [64]–[67] seek to unify locomotion, terrain adaptation, and collision avoidance with exteroceptive data and navigation-based objectives. Despite their conceptual elegance, these frameworks often encounter practical bottlenecks. Specifically, the update frequency of exteroceptive perception typically cannot match the high-rate requirements of locomotion control. Furthermore, high-frequency perceptual processing often introduces significant sensor noise and latency. In addition, a reliance on static, pre-built elevation maps restricts the robot’s adaptability to unexplored or dynamic environments.

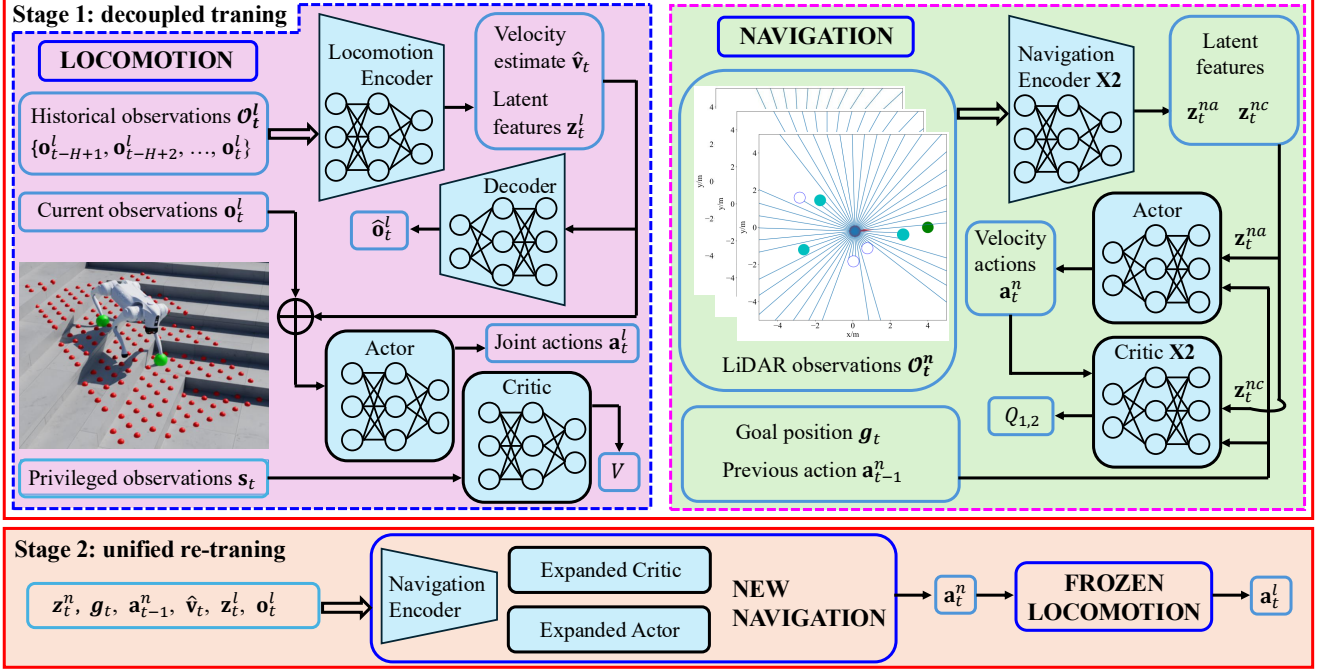


Fig. 2. Overall framework with a two-stage training architecture. In the first stage, a quadrupedal locomotion policy and a social navigation policy are trained separately. In the second stage, these two policies are unified into a single quadrupedal navigation policy, which is further retrained in uneven and socially interactive environments.

To mitigate the dependence on high-frequency perception while accounting for locomotion constraints, frameworks such as Vision and Proprioception for Navigation (VP-Nav) [68] first predict potential collisions and falls based on proprioceptive states, subsequently leveraging these predictions for low-frequency navigation tasks. Similarly, Visual Navigation and Locomotion (ViNL) [69] employs a teacher–student paradigm to distill exteroceptive data into a unified policy. Despite these advancements, current research in quadrupedal navigation is largely restricted to static environments, where latent environmental features are relatively stable and easy to extract. However, the most compelling applications for quadrupedal robots involve human-centric tasks, such as last-mile delivery and autonomous surveillance, which necessitate agile, reactive interactions with dynamic pedestrians across irregular terrains, including staircases, inclines, and unpaved surfaces.

III. FRAMEWORK AND PROBLEM FORMULATION

A. Overall Framework

The proposed framework, illustrated in Fig. 2, utilizes a two-stage training architecture comprising three DRL modules. During the first stage, two specialized policies are developed in parallel:

Locomotion controller: This controller is trained using high-fidelity and full-body quadruped models in IsaacSim [70] to ensure robust locomotion across uneven terrains.

Navigation policy: This policy is trained in socially interactive environments using a simplified CoM model governed by differential kinematics and associated kinematics constraints.

In the second stage, these policies are integrated into a unified architecture. This combined pipeline is then fine-tuned

as the quadruped robot learns to navigate challenging terrains while simultaneously performing reactive collision avoidance with dynamic pedestrians and static obstacles.

B. Problem Formulation

We formulate quadrupedal locomotion, social navigation, and integrated quadrupedal navigation in uneven, socially interactive environments as Partially Observable Markov Decision Processes (POMDPs). A POMDP is defined by the tuple $\mathcal{P} = \langle S, A, T, R, \Omega, O, \gamma \rangle$, where S denotes the state space, A the action space, $T(s'|s \in S, a \in A)$ the probability of transitioning to state s' from state s after taking action a , $R(s, a)$ the reward for taking action a in state s , Ω the observation space, $O(o|s', a)$ the probability of receiving observation o after taking action a and arriving in state s' , and γ the reward discount factor.

To solve these POMDPs without explicit knowledge of the underlying transition and observation models (T, O), we employ model-free RL to iteratively optimize the policy through environmental interaction. We define the interaction between the agent and the environment as follows:

$$s_t \in S \xrightarrow{a_t \in A} s_{t+1} \in S, r_t \in R.$$

The agent aims to learn a policy $\pi(a_t|s_t)$ that maximizes the expected cumulative reward:

$$J(\pi) = \mathbb{E}_\pi \left[\sum_{t=0}^{\infty} \gamma^t r_t \right]. \quad (1)$$

We employ a suite of specialized DRL algorithms to optimize the policies across our multi-stage framework, encompassing

quadrupedal locomotion, social navigation, and their subsequent integration.

To maintain consistency across our multi-task framework, we adopt a standardized notation. Since the three DRL pipelines share a common POMDP formulation, we utilize superscripts $\{l, n, u\}$ to distinguish between locomotion, social navigation, and unified navigation in uneven and socially interactive environments, respectively. Furthermore, within the Actor–Critic (AC) framework, we employ superscripts $\{a, c\}$ to differentiate between the actor and critic state spaces. Under this convention, for example, $s_t^{u,c}$ represents the state of the critic in the unified navigation module at time t .

IV. QUADRUPEDAL LOCOMOTION

Our locomotion controller, TRANS-Loco, builds upon the DreamWaQ [53] architecture. While maintaining the core DRL workflow, we significantly enhance the system by redesigning the encoder network and refining the reward structures to improve stability and gait efficiency.

A. Observations and States

Precise knowledge of terrain geometry and full-body contact dynamics is essential for stable quadrupedal locomotion on irregular surfaces. However, real-world exteroceptive sensing is inherently noisy and requires substantial computational overhead to maintain high-frequency, real-time elevation mapping. Furthermore, a strict reliance on pre-built terrain maps compromises the robot's adaptability to unforeseen or dynamic environments. To circumvent these limitations, we adopt an asymmetric actor–critic architecture [71]. This framework allows the critic to leverage privileged terrain and contact data during training, while the actor learns to infer these implicit environmental features solely from proprioceptive history, ensuring robust deployment on hardware without the need for explicit mapping.

During the training phase, the critic network has access to the full simulation state, including both proprioceptive observations \mathbf{o}_t^l and privileged exteroceptive information. Since the critic is discarded prior to real-world deployment, this asymmetric information flow allows it to provide more accurate value estimations during policy optimization. The proprioceptive observation vector, $\mathbf{o}_t^l \in \mathbb{R}^{45}$, provides the robot with its current kinematic and dynamic status and is defined as:

$$\mathbf{o}_t^l = [\omega_t, \mathbf{g}_t, \mathbf{c}_t, \theta_t, \dot{\theta}_t, \mathbf{a}_{t-1}^l], \quad (2)$$

where $\omega_t \in \mathbb{R}^3$ represents the base angular velocity, $\mathbf{g}_t \in \mathbb{R}^3$ is the gravity vector projected into the robot's base frame, $\mathbf{c}_t \in \mathbb{R}^3$ denotes the target velocity command provided by the high-level planner, $\theta_t \in \mathbb{R}^{12}$ and $\dot{\theta}_t \in \mathbb{R}^{12}$ respectively correspond to the joint positions and velocities, and $\mathbf{a}_{t-1}^l \in \mathbb{R}^{12}$ are the angular offsets relative to the default standing configuration from the previous time step, included to promote temporal smoothness in control.

The exteroceptive component of the privileged state incorporates a local terrain height map, $\mathcal{H}_t \in \mathbb{R}^{187}$, and full-body contact forces, $\mathcal{C}_t \in \mathbb{R}^{51}$. As illustrated in Fig. 3(a), the height

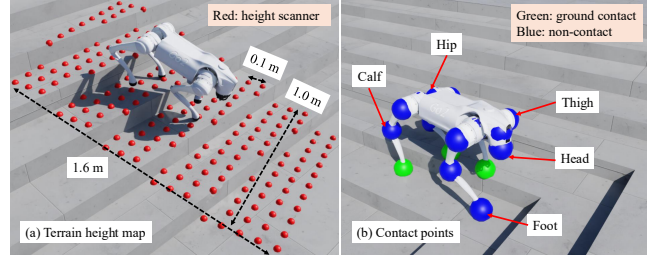


Fig. 3. Terrain height map and contact points visualized in IsaacSim.

map is sampled over a 1.6×1.0 m grid centered on the robot with a resolution of 0.1 m. To capture comprehensive interaction dynamics, we monitor 17 distinct body contact points, as depicted in Fig. 3(b). These points include the four feet, calves, thighs, and hips, alongside the head. For each contact point, the critic receives the three-dimensional force components (x, y, z) in the robot frame.

To account for the inherent noise and estimation drift associated with the body linear velocity $\mathbf{v}_t \in \mathbb{R}^3$ on physical hardware, we exclude it from the actor's observation vector \mathbf{o}_t^l . Instead, we treat \mathbf{v}_t as a privileged component available only during training. This ensures the locomotion policy remains robust to velocity estimation errors while allowing the critic to utilize the ground-truth velocity for accurate value estimation. In summary, the comprehensive critic state is defined as:

$$\mathbf{s}_t^{l,c} = [\mathbf{o}_t^l, \mathcal{H}_t, \mathcal{C}_t, \mathbf{v}_t] \in \mathbb{R}^{286}. \quad (3)$$

To ensure reliable and efficient real-world deployment, the actor network, which constitutes the final onboard locomotion policy, excludes the privileged variables \mathcal{H}_t , \mathcal{C}_t , and \mathbf{v}_t . Instead, as depicted in Fig. 2, the actor relies on a temporal encoder to extract a latent representation $\mathbf{z}_t^l \in \mathbb{R}^{16}$ that implicitly encodes terrain geometry and contact dynamics. Simultaneously, the encoder provides an estimate of the body linear velocity, $\hat{\mathbf{v}}_t \in \mathbb{R}^3$. These features are derived from a historical observation buffer, \mathcal{O}_t^l , defined as:

$$\mathcal{O}_t^l = [\mathbf{o}_{t-H+1}^l, \mathbf{o}_{t-H+2}^l, \dots, \mathbf{o}_t^l] \in \mathbb{R}^{10 \times 45}, \quad (4)$$

where the history length is set to $H = 10$. Consequently, the actor state, $\mathbf{s}_t^{l,a}$, is formulated as:

$$\mathbf{s}_t^{l,a} = [\mathbf{o}_t^l, \mathbf{z}_t^l, \hat{\mathbf{v}}_t] \in \mathbb{R}^{64}. \quad (5)$$

By utilizing $\mathbf{s}_t^{l,a}$, the actor can effectively navigate complex environments by inferring critical physical properties from its own motion history, bypassing the need for high-frequency exteroceptive mapping.

B. Locomotion Actions

The locomotion actions are defined as $\mathbf{a}_t^l \in \mathbb{R}^{12}$, representing the angular offsets relative to the default standing configuration, θ_{stand} . To ensure mechanical safety and maintain gait stability, the absolute magnitude of each action component is capped at 0.25 rad. The target joint positions, θ_{des} , are calculated as:

$$\theta_{\text{des}} = \theta_{\text{stand}} + \mathbf{a}_t^l. \quad (6)$$

To track these setpoints, a low-level Proportional-Derivative (PD) controller computes the required joint torques τ_t :

$$\tau_t = \mathbf{K}_p(\theta_{\text{des}} - \theta_t) - \mathbf{K}_d\dot{\theta}_t, \quad (7)$$

where \mathbf{K}_p and \mathbf{K}_d denote the diagonal matrices of proportional and derivative gains, respectively, and $\dot{\theta}_t$ represents the current joint velocities. This hierarchical control structure enables the RL policy to operate at a lower frequency while the PD controller ensures high-frequency tracking and joint impedance.

C. Networks

As illustrated in Fig. 2, the TRANS-Loco architecture is composed of three primary modules: the actor network, the critic network, and a temporal auto-encoder. The specifications for these networks are detailed in APPENDIX A.

Actor and critic networks: Both utilize Multi-Layer Perceptrons (MLPs) with an identical hidden layer configuration to maintain representational parity. Their architectures diverge only at the output stage to accommodate their respective tasks. The actor network, or policy $\pi_{\phi^l}(\mathbf{a}_t^l | \mathbf{s}_t^{l,a})$, infers the joint action \mathbf{a}_t^l , while the critic network $V_{\psi^l}(\mathbf{s}_t^{l,c})$ estimates the state-value function for policy evaluation.

Temporal auto-encoder: This module serves as the core for latent feature extraction. The encoder employs a hybrid structure of Convolutional Neural Networks (CNNs) and MLPs to process the historical observation buffer \mathcal{O}_t^l , while the decoder consists of a two-layer MLP designed to reconstruct the proprioceptive state $\hat{\mathbf{o}}_t^l$. We employ a variational temporal encoder $f_{\varphi^l}(\mathcal{O}_t^l)$ to extract the estimated body linear velocity $\hat{\mathbf{v}}_t^l$ alongside latent terrain and contact features \mathbf{z}_t^l . Subsequently, a decoder network $f_{\rho}(\mathbf{z}_t^l, \hat{\mathbf{v}}_t^l)$ reconstructs the current observation as $\hat{\mathbf{o}}_t^l$. The network parameters are updated jointly via a reconstruction loss between $\hat{\mathbf{o}}_t^l$ and the ground-truth observation \mathbf{o}_t^l . Furthermore, an estimation loss is formulated using $\hat{\mathbf{v}}_t^l$ and the privileged linear velocity data provided by the simulator.

Activation and layers: All hidden layers across the three networks employ the Exponential Linear Unit (ELU) activation function to ensure smooth gradient flow. In contrast, the output layers remain linear to allow for unconstrained regression of actions, values, and reconstructed observations.

The network parameters $\{\phi^l, \psi^l, \varphi^l, \rho\}$ are optimized via a multi-objective loss function. This objective integrates the Proximal Policy Optimization (PPO) loss [72] for locomotion control, a mean square error (MSE) term for velocity estimation, and a Variational Autoencoder (VAE) loss [73] to facilitate representation learning.

D. Rewards

The reward structure for TRANS-Loco builds upon the DreamWaQ framework [53], with refinements specifically engineered to improve learning efficiency and cross-platform generalizability. As summarized in TABLE I, the total reward consists of task rewards, which penalize deviations from the commanded velocity, and stability rewards, which promote natural gait patterns and structural safety.

TABLE I
REWARD FUNCTION FOR QUADRUPEDAL LOCOMOTION

Reward	Equation (r_i)	Weight (w_i)
Linear vel track	$\exp\{-4(\mathbf{v}_{xy}^{\text{cmd}} - \mathbf{v}_{xy})^2\}$	1.5
Angular vel track	$\exp\{-4(w_z^{\text{cmd}} - w_z)^2\}$	0.75
Linear vel (z)	v_z^2	-2.0
Angular vel (xy)	w_{xy}^2	-0.05
Torque	τ^2	-2×10^{-4}
Angular acceleration	$\ddot{\theta}^2$	-2.5×10^{-7}
Action rate	$(\mathbf{a}_t^l - \mathbf{a}_{t-1}^l)^2$	-0.01
Feet air time	$(\mathbf{t}_a^{\text{last}} - 0.5) \cdot \mathbf{t}_c^{\text{check}} \cdot \ \mathbf{v}_{xy}^{\text{cmd}}\ _2$	0.01

In our formulation, the operator $\exp(\cdot)$ denotes the exponential function, while superscripts $(\cdot)^{\text{cmd}}$ distinguish target values from measured states. All kinematic variables are defined in the robot's local body frame, where the x -axis and z -axis point forward and upward, respectively. Specifically:

- \mathbf{v}_{xy} and w_{xy} represent the linear and angular velocities in the horizontal plane. The commands for \mathbf{v}_{xy} are randomly set from -1.0 to 1.0 m/s during training.
- v_z and w_z denote the vertical linear velocity and yaw rate. The command for w_z ranges from -1.0 to 1.0 rad/s.
- τ and $\ddot{\theta}$ correspond to the applied joint torques and joint accelerations, respectively.

To regulate gait timing and contact dynamics, we utilize $\mathbf{t}_a^{\text{last}}$ to denote the flight duration prior to the most recent contact event. Additionally, the boolean operator $\mathbf{t}_c^{\text{check}}$ determines whether a foot has established ground contact within the preceding control interval $\Delta t^l = 0.02$ s (50 Hz).

The total reward is computed as:

$$r_t^l(\mathbf{s}_t^{l,c}, \mathbf{a}_t^l) = \sum r_i \cdot w_i \cdot \Delta t^l, \quad (8)$$

where i is the index of each reward shown in TABLE I.

E. Curriculum Learning and Domain Randomization

The training environment encompasses a diverse range of challenging topographies, including flat ground, inclines, stairs, rough terrain, and stepped grids, as illustrated in Fig. 1. The geometric complexity is parameterized as follows:

- Slopes: Angles ranging from 0° to 23° .
- Stairs: Step heights varying within $[0.05, 0.12]$ m.
- Rough surfaces: Stochastic height noise ranging from 0.01 to 0.06 m.
- Stepped grids: Discrete height variations between 0.025 and 0.1 m.

To ensure stable policy convergence across these diverse conditions, we employ curriculum learning to adaptively modulate terrain difficulty. The curriculum operates on a performance-based heuristic: the terrain level is incremented upon successful and stable traversal of the current difficulty, while a failure to maintain stability triggers a reduction in difficulty. This progressive approach allows the agent to build foundational gait patterns before tackling the most extreme environmental constraints.

TABLE II
LOCOMOTION DOMAIN RANDOMIZATION

Type	Domain	Noise
System dynamics	Friction coefficient	[0.65, 1.25]
	Body mass	[-1.0, 3.0] kg
	CoM xy	[-0.05, 0.05] m
Observations	CoM z	[-0.01, 0.01] m
	Body linear vel \mathbf{v}_t	[-0.1, 0.1] m/s
	Body angular vel $\boldsymbol{\omega}_t$	[-0.2, 0.2] rad/s
	Projected gravity \mathbf{g}_t	[-0.1, 0.1] m
	Joint position θ_t	[-0.01, 0.01] rad
	Joint velocity $\dot{\theta}_t$	[-1.5, 1.5] rad/s
Reset	Height map \mathcal{H}_t	[-0.1, 0.1] m
	Initial joint offset	[-0.1, 0.1] rad

Despite the fidelity of modern simulators, significant discrepancies between simulated environments and the physical world, termed the sim-to-real gap, can compromise the deployment of locomotion policies on real hardware. To bridge this gap, we employ Domain Randomization (DR), a technique that exposes the policy to a wide distribution of physical parameters during training.

Our DR implementation, detailed in TABLE II, is modeled after established benchmarks in robust locomotion [45], [53], [54]. We introduce stochasticity by sampling from uniform distributions and applying these perturbations to:

- System dynamics: Randomizing default robot parameters such as body mass, center of mass (CoM) positions, and ground friction coefficients.
- Observations: Injecting noise into proprioceptive and terrain height measurements.
- Reset: Randomizing initial joint angles to start from diverse initial robot states.

In summary, the locomotion framework, TRANS-Loco, is illustrated in **Algorithm 1**.

V. SOCIAL NAVIGATION

In parallel with TRANS-Loco, we propose a straightforward framework for social navigation, termed TRANS-Nav. This module directly maps transformed LiDAR scans to robot actions while adhering to the velocity constraints of differential-drive kinematics.

A. Social Navigation Actions and Kinematics

Actions. To simplify the navigation task and improve stability, we model the quadruped robot as a circular ego-agent with radius r^{agent} . The agent's movement is governed by differential-drive kinematics, with linear velocity $v^n \in [0, v_{\max}]$ and angular velocity $w^n \in [-w_{\max}, w_{\max}]$. Notably, we exclude lateral (y -direction) velocity commands; our empirical observations indicated that lateral movement frequently caused leg self-collisions, particularly when traversing challenging terrains. Accordingly, the navigation action space is defined as:

$$\mathbf{a}_t^n = [v_t^n, w_t^n]^T. \quad (9)$$

Algorithm 1 TRANS-Loco

```

1: Initialize: itr  $\leftarrow 1$ , randomize masses and CoMs for  $N_r$  quadruped robots in IsaacSim
2: Reset: Robot pose in the world frame, terrain level, PPO episode buffer  $\mathcal{D}$ , reset  $\leftarrow \text{False}$ ,  $t \leftarrow 0$ 
3: Observe:  $\mathbf{o}_t^l, \mathbf{s}_t^{l,c}, \mathcal{O}_t^l$ 
4: while itr  $\leq \mathcal{I}$  do
5:   Compute  $\hat{\mathbf{v}}_t$  and  $\mathbf{z}_t^l$  with  $f_{\varphi^l}(\mathcal{O}_t^l)$ 
6:   Construct  $\mathbf{s}_t^{l,a}$  with  $\mathbf{o}_t^l$ ,  $\hat{\mathbf{v}}_t$  and  $\mathbf{z}_t^l$ 
7:   Sample an action  $\mathbf{a}_t^l$  with  $\pi_{\phi^l}(\mathbf{s}_t^{l,a})$ 
8:   Execute one step with the action  $\mathbf{a}_t^l$  in IsaacSim
9:    $t \leftarrow t + 1$ 
10:  Observe
11:  Calculate  $r_t^l$  using Eq. (8)
12:  Estimate the value function  $V_{\psi^l}(\mathbf{s}_t^{l,c})$ 
13:  if robot fall or episode timeout then
14:    reset  $\leftarrow \text{True}$ 
15:  end if
16:  Fill  $\mathcal{D}$  with  $r_t^l, \mathbf{a}_t^l, \mathbf{o}_t^l, \mathbf{s}_t^{l,c}, \mathcal{O}_t^l, V_{\psi^l}(\mathbf{s}_t^{l,c})$  and reset
17:  if reset then
18:    Sample batches from  $\mathcal{D}$ 
19:    Update network parameters  $\phi^l, \psi^l, \varphi^l$ , and  $\rho$  via PPO [72] and VAE [73]
20:    Update terrain level via curriculum learning
21:  Reset
22:  Observe
23:  itr  $\leftarrow$  itr + 1
24:  end if
25: end while

```

We set $v_{\max} = 0.5$ m/s and $w_{\max} = 1.0$ rad/s.

Differential kinematics. Given the action \mathbf{a}_t^n and the current ego-agent state $\mathbf{x}_t = [x_t, y_t, \theta_t^n]^T$, where (x_t, y_t) and θ_t^n represent the position and orientation in the 2D global frame, the state is updated according to the differential-drive kinematic model:

$$\mathbf{x}_{t+1} = \mathbf{x}_t + \mathbf{B} \mathbf{a}_t^n \Delta t^n, \quad (10)$$

where $\Delta t^n = 0.2$ s is the motion planning period for social navigation, and \mathbf{B} denotes the control matrix:

$$\mathbf{B} = \begin{bmatrix} \cos \theta_t^n & 0 \\ \sin \theta_t^n & 0 \\ 0 & 1 \end{bmatrix}.$$

Remark 1: We employ differential-drive kinematics for social navigation in the initial training stage rather than modeling full-body quadrupedal dynamics. This abstraction offers high computational efficiency and provides a “warm start” for the subsequent stage, significantly accelerating overall learning. Additionally, this kinematic simplification facilitates direct comparisons between our learning-based policies and a variety of traditional model-based motion planners.

B. Observations and States

To capture the complex dynamics of pedestrian and obstacle interactions, we introduce a novel representation termed *transformed LiDAR scans*. As shown in Fig. 4, the raw LiDAR

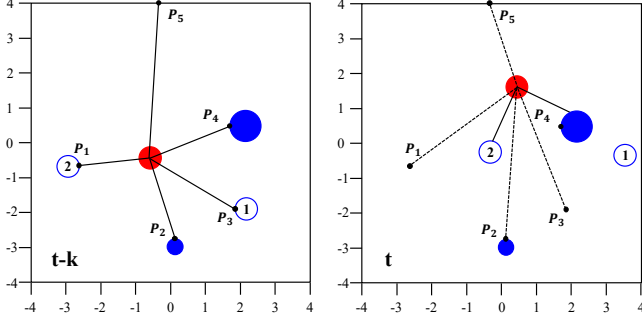


Fig. 4. LiDAR scan transformation. The red filled circle represents the ego-agent, blue filled circles denote static obstacles of varying sizes, and blue hollow circles indicate pedestrians with a fixed radius. The left panel shows the LiDAR scan (solid beams) at time $t - k$, while the right panel illustrates the scan (solid beams) at the current time t . Dashed lines in the right panel correspond to the transformed LiDAR beams from $t - k$ to t . Each point P_i retains the same global position in both panels.

observation $\mathbf{o}_t^n \in \mathbb{R}^{1800}$ provides a 360° field of view. To incorporate temporal context, we maintain a buffer of historical scans. For a scan captured at time $t - k$, the local position of each interaction point P_i in the robot's coordinate frame is denoted as $\mathbf{p}_{t-k}^{i\text{-loc}} = [x_{t-k}^{i\text{-loc}}, y_{t-k}^{i\text{-loc}}]^T$:

$$\begin{aligned} \vartheta_{t-k}^i &= 2\pi \cdot \frac{i}{N}, i \in \{1, 2, \dots, n\}, \\ x_{t-k}^{i\text{-loc}} &= r_{t-k}^i \cos \vartheta_{t-k}^i, \quad y_{t-k}^{i\text{-loc}} = r_{t-k}^i \sin \vartheta_{t-k}^i, \end{aligned} \quad (11)$$

where $N = 1800$ denotes the number of LiDAR beams, ϑ_{t-k}^i is the beam angle, and r_{t-k}^i is the corresponding range measurement. At time $t - k$, given the global position and orientation of the ego-agent $\mathbf{p}_{t-k}^{\text{ego}} = [x_{t-k}, y_{t-k}]^T$ and θ_{t-k}^n , we compute the global position of each interaction point P_i , denoted as $\mathbf{p}_{t-k}^{i\text{-glob}} = [x_{t-k}^{i\text{-glob}}, y_{t-k}^{i\text{-glob}}]^T$:

$$\mathbf{p}_{t-k}^{i\text{-glob}} = \mathbf{p}_{t-k}^{\text{ego}} + \mathbf{R}(\theta_{t-k}^n) \mathbf{p}_{t-k}^{i\text{-loc}}, \quad (12)$$

where $\mathbf{R}(\theta_{t-k}^n)$ is the rotation matrix:

$$\mathbf{R}(\theta_{t-k}^n) = \begin{bmatrix} \cos \theta_{t-k}^n & -\sin \theta_{t-k}^n \\ \sin \theta_{t-k}^n & \cos \theta_{t-k}^n \end{bmatrix}.$$

Given the current ego-agent position and orientation $\mathbf{p}_t^{\text{ego}} = [x_t, y_t]^T$ and θ_t^n on the global frame, the position of P_i on the current robot frame can be obtained by inverting Eq. (12):

$$\tilde{\mathbf{p}}_{t-k}^{i\text{-loc}} = \mathbf{R}^{-1}(\theta_t^n) (\mathbf{p}_{t-k}^{i\text{-glob}} - \mathbf{p}_t^{\text{ego}}), \quad (13)$$

where $\tilde{\mathbf{p}}_{t-k}^{i\text{-loc}} = [\tilde{x}_{t-k}^{i\text{-loc}}, \tilde{y}_{t-k}^{i\text{-loc}}]^T$ denotes the position of P_i on the current ego-agent frame. Finally, we reconstruct the LiDAR scan as:

$$\tilde{r}_{t-k}^i = \|\tilde{\mathbf{p}}_{t-k}^{i\text{-loc}}\|_2, \quad (14)$$

where \tilde{r}_{t-k}^i denotes the range from the ego-agent to P_i at the current time step. Therefore, the transformed LiDAR scan is represented as:

$$\tilde{\mathbf{o}}_{t-k}^n = \{\tilde{r}_{t-k}^i | i = 1, 2, \dots, N\}^T. \quad (15)$$

Together with the current LiDAR scan \mathbf{o}_t^n , we represent the final observation as:

$$\mathcal{O}_t^n = [\tilde{\mathbf{o}}_{t-K+1}^n, \dots, \tilde{\mathbf{o}}_{t-1}^n, \mathbf{o}_t^n] \in \mathbb{R}^{6 \times 1800}, \quad (16)$$

where $K = 6$ is the total number of LiDAR scans, with the most recent scan kept in its original form and the previous $K - 1$ scans transformed into the current ego-agent frame.

By transforming historical LiDAR scans into the current robot frame, we filter out the ego-agent's motion, allowing the network to isolate and represent the independent movements of pedestrians. Furthermore, this transformation aids in identifying static obstacles, as their re-projected points remain spatially consistent across time steps. Our experiments, detailed in Section VIII-B, demonstrate that this representation significantly enhances social navigation performance compared to the use of raw LiDAR scans.

Given the observations \mathcal{O}_t^n , we extract latent states $\mathbf{z}_t^{n,a} \in \mathbb{R}^{50}$ and $\mathbf{z}_t^{n,c} \in \mathbb{R}^{50}$ for the actor and critic using two encoders with identical architectures. The navigation task is guided by the goal position in the robot frame, $\mathbf{g}_t = [r_t^{\text{goal}}, \theta_t^{\text{goal}}]$, where r_t^{goal} and θ_t^{goal} represent the goal distance and relative orientation in the ego-agent frame, respectively. To account for reciprocal interactions, where the ego-agent's movements influence pedestrian behavior, the previous action \mathbf{a}_{t-1}^n is also included in the state representation. Therefore, the combined state is represented as:

$$\mathbf{s}_t^{n,*} = [\mathbf{z}_t^{n,*}, \mathbf{g}_t, \mathbf{a}_{t-1}^n] \in \mathbb{R}^{54}, * \in \{a, c\}. \quad (17)$$

In contrast to the locomotion module's use of asymmetric states, the state \mathbf{s}_t^n for TRANS-Nav is symmetric for both the actor and critic networks. This design choice stems from the fact that stable, low-frequency LiDAR scans are more readily accessible in real-world scenarios than precise terrain height maps or full-body contact data. Consequently, there is no requirement to distill privileged sensing data into the actor network for the navigation task.

C. Networks

The neural network architecture for TRANS-Nav comprises three primary components: the actor and critic networks, implemented as MLPs, and the encoder network, which utilizes a combination of CNNs and MLPs. Comprehensive structural details are summarized in APPENDIX B. All hidden layers employ the Rectified Linear Unit (ReLU) activation function, while the output layers remain linear.

The actor network $\pi_{\phi^n}(\mathbf{a}_t^n | \mathbf{s}_t^n)$ parameterizes a normal distribution by outputting the mean and log-variance of the action \mathbf{a}_t^n . Since we employ the Soft Actor-Critic (SAC) algorithm [74], the critic architecture differs from the locomotion module. Specifically, the critic estimates the action-value function $Q(\mathbf{s}_t^n, \mathbf{a}_t^n)$, taking both the state and action as inputs. To mitigate value overestimation, we utilize twin critics ($Q_{\psi_1^n}$ and $Q_{\psi_2^n}$) alongside two corresponding target critics ($Q_{\bar{\psi}_1^n}$ and $Q_{\bar{\psi}_2^n}$), which stabilize training by smoothing the bootstrapped targets. Latent features for the actor and critic, denoted as $\mathbf{z}_t^{n,a}$ and $\mathbf{z}_t^{n,c}$, are extracted from two encoder networks $f_{\varphi^{n,a}}(\mathcal{O}_t^n)$ and $f_{\varphi^{n,c}}(\mathcal{O}_t^n)$, respectively:

$$\mathbf{z}_t^{n,a} = f_{\varphi^{n,a}}(\mathcal{O}_t^n), \quad (18a)$$

$$\mathbf{z}_t^{n,c} = f_{\varphi^{n,c}}(\mathcal{O}_t^n). \quad (18b)$$

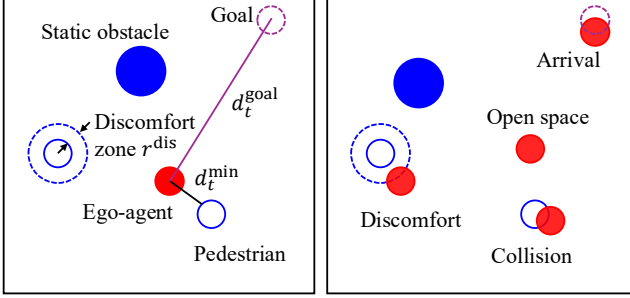


Fig. 5. Reward structure and scenarios. The left panel illustrates the geometric representation used for defining the reward function, while the right panel depicts four possible ego-agent scenarios: collision, goal arrival, discomfort, and open space.

The network parameters ϕ^n , $\psi_{1,2}^n$, $\bar{\psi}_{1,2}^n$, $\varphi^{n,a}$, and $\varphi^{n,c}$ are updated using the SAC algorithm [74].

Remark 2: We employ the SAC algorithm because, in our empirical evaluations, PPO failed to converge on a feasible social navigation policy. Furthermore, we utilize only the encoder network; incorporating a decoder within an auto-encoder framework did not provide additional improvements to learning efficiency or navigation performance.

Remark 3: We only update the parameters of the CNN encoder together with the critic networks, and then copy the updated parameters from $\varphi^{n,c}$ to $\varphi^{n,a}$. This approach avoids duplicating CNN updates in the actor network, whose gradients are typically much noisier, thereby improving learning stability.

D. Rewards

Since the navigation task prioritizes collision avoidance and goal reaching, the reward function is defined based on four distinct scenarios: goal arrival, collision, discomfort, and open space, as illustrated in Fig. 5:

$$r_t^n = \begin{cases} 0.5, & d_t^{\text{goal}} \leq r_{\text{robot}}, \\ -0.5, & d_t^{\text{min}} \leq r_{\text{robot}}, \\ r_t^{\text{dis}} + r_t^{\text{goal}}, & r_{\text{robot}} < d_t^{\text{min}} \leq r_{\text{robot}} + r_{\text{dis}}, \\ r_t^{\text{goal}}, & r_{\text{robot}} + r_{\text{dis}} < d_t^{\text{min}}, \end{cases} \quad (19)$$

where r_{robot} denotes the radius of the ego-agent, d_t^{goal} is the distance between the goal and the ego-agent at time t , d_t^{min} represents the minimum range of the current LiDAR scan, and r_{dis} defines the annulus width of the discomfort zone, as illustrated in Fig. 5. The discomfort penalty r_t^{dis} and the goal proximity reward r_t^{goal} are computed as:

$$\begin{aligned} r_t^{\text{dis}} &= w^{\text{dis}} \cdot (d_t^{\text{min}} - r_{\text{robot}} - r_{\text{dis}}), \\ r_t^{\text{goal}} &= w^{\text{goal}} \cdot (d_{t-1}^{\text{goal}} - d_t^{\text{goal}}), \end{aligned} \quad (20)$$

where w^{dis} and w^{goal} are the weights for the discomfort penalty and the goal proximity reward, respectively. These terms are designed to further ensure safety and to encourage motion toward the final goal. In this work, we set $r_{\text{robot}} = 0.3$ m, $r_{\text{dis}} = 0.5$ m, $w^{\text{dis}} = 0.4$, and $w^{\text{goal}} = 1.4$.

E. Pedestrian Motions and Domain Randomization

Interactive pedestrian motions are generated using ORCA [16], [17], a framework widely adopted in learning-based navigation research [11], [25]–[29]. Unlike standard setups where pedestrians always avoid the robot, we modify the simulation so that pedestrians ignore the ego-agent if their current speed is less than 1.5 times the agent's speed. This modification forces the ego-agent to actively navigate around pedestrians, ensuring the policy learns proactive avoidance rather than relying on the pedestrians' reciprocal collision avoidance strategies.

Since ORCA serves as an ideal multi-agent motion planner for generating pedestrian velocities, we perturb these velocities with uniform noise $\in [-0.15, 0.15]$ m/s to facilitate sim-to-real transfer. Similarly, we apply uniform noise $\in [-0.03, 0.03]$ m to the positions of static obstacles. Because the LiDAR scan construction is derived from these perturbed pedestrian and obstacle positions, no additional domain randomization is applied directly to the LiDAR observations.

Algorithm 2 TRANS-Nav

```

1: Initialize:  $\text{itr} \leftarrow 1$ , SAC experience pool  $\mathcal{D}$ 
2: Reset: ego-agent pose in the world frame, number of static
   obstacles and pedestrians, positions and sizes of static
   obstacles, pedestrian positions,  $\text{reset} \leftarrow \text{False}$ ,  $t \leftarrow 0$ 
3: Observe:  $\mathbf{a}_{t-1}^n$ ,  $\mathbf{g}_t$  and  $\mathcal{O}_t^n$ 
4: while  $\text{itr} \leq \mathcal{I}$  do
5:   Compute  $\mathbf{z}_t^{n,a}$  using Eq. (18a) with  $\mathcal{O}_t^n$ 
6:   Form  $\mathbf{s}_t^{n,a}$  with  $\mathbf{z}_t^{n,a}$ ,  $\mathbf{a}_{t-1}^n$  and  $\mathbf{g}_t$ 
7:   Sample action  $\mathbf{a}_t^n$  with  $\pi_{\phi^n}$  and  $\mathbf{s}_t^{n,a}$ 
8:   Rollout one step with the action  $\mathbf{a}_t^n$ 
9:    $t \leftarrow t + 1$ 
10:  Observe
11:  Calculate reward  $r_t^n$  using Eq. (19)
12:  if arrival or collision or episode timeout then
13:     $\text{reset} \leftarrow \text{True}$ 
14:  end if
15:  Fill  $\mathcal{D}$  with  $r_t^n$ ,  $\mathbf{a}_{t-1}^n$ ,  $\mathbf{g}_t$ ,  $\mathcal{O}_t^n$  and  $\text{reset}$ 
16:  Sample batches from  $\mathcal{D}$ 
17:  Update network parameters  $\phi^n$ ,  $\psi_{1,2}^n$ ,  $\varphi^{n,a}$  and  $\varphi^{n,c}$ 
   using SAC [74]
18:   $\text{itr} \leftarrow \text{itr} + 1$ 
19:  if  $\text{reset}$  then
20:    Reset
21:    Observe
22:  end if
23: end while

```

A summary of the social navigation workflow, TRANS-Nav, is presented in **Algorithm 2**.

VI. UNIFIED QUADRUPEDAL NAVIGATION

To incorporate quadrupedal dynamics, kinematic constraints, terrain information, and body contact states, we propose a unified architecture that embeds the locomotion policy developed in Section IV into the social navigation strategy introduced in Section V.

A. Expansion of Social Navigation

The unified architecture, illustrated in Fig. 2, extends the social navigation framework with the following enhancements and modifications:

- The simulation employs a high-fidelity quadruped robot model within IsaacSim (see Fig. 1), replacing the simplified differential kinematics defined in Eq. (10). This configuration enables the framework to fully capture complex quadrupedal dynamics, such as inertia and gait stability, during social navigation tasks. Furthermore, the robot is randomly initialized on uneven terrain, as shown in Fig. 1, ensuring that terrain-specific constraints and proprioceptive feedback are directly integrated into the learning process.
- We constrain the lateral velocity v_y to zero because our social navigation action space is restricted to linear and angular velocities (v_x, ω). Our empirical observations indicated that lateral movement frequently caused leg self-collisions, particularly when traversing challenging terrains..
- To facilitate the integration, we freeze the locomotion policy pre-trained in Section VI-A, with the lateral velocity command v_y disabled, and interface it directly along with TRANS-Nav.
- The unified state space integrates the state representations from both the locomotion controller and the social navigation policy, and is defined as follows:

$$\mathbf{s}_t^{u,*} = [\mathbf{z}_t^{n,*}, \mathbf{g}_t, \mathbf{a}_{t-1}^n, \hat{\mathbf{v}}_t, \mathbf{z}_t^l, \mathbf{o}_t^l] \in \mathbb{R}^{118}, * \in \{a, c\}. \quad (21)$$

To account for the frequency discrepancy between the navigation and locomotion layers, we update $\hat{\mathbf{v}}_t$, \mathbf{z}_t^l , and \mathbf{o}_t^l only after the locomotion policy has executed 10 control cycles. Both $\hat{\mathbf{v}}_t$ and \mathbf{z}_t^l are latent features derived from the previous 10 observations, as defined in Eq. (4). This architecture allows us to omit explicit historical locomotion states, relying instead on the latent features from the most recent control step. This expanded state representation effectively integrates terrain awareness and implicit body contact information into the quadrupedal navigation process.

- To incorporate quadrupedal locomotion safety into the reward function, a penalty of -0.5 is added to Eq. (19) whenever the robot falls, such as through illegal body contact with the ground. This additional term encourages the policy to prioritize stable locomotion, thereby enhancing the overall stability of quadrupedal social navigation.
- To facilitate more stable sim-to-real transfer, we penalize abrupt changes in angular velocity. Consequently, an additional regularization term is incorporated into Eq. (19):

$$r = -0.01 \cdot |w_t^n - w_{t-1}^n|. \quad (22)$$

- The networks are expanded to accommodate the unified state $\mathbf{s}_t^{u,*}$. With the input dimensionality increasing to 118, the input shapes of the expanded networks are updated to (118,) for the actor and (120,) for the critic. Consequently, the network parameters defined in Section V-C are scaled to match these expanded input dimensions.

- To prevent jitter and ensure stable motion at low speeds, the linear and angular velocities are set to zero if the linear velocity commanded by TRANS-Nav falls below 0.3 m/s. This thresholding logic results in the following clipped action definition:

$$\mathbf{a}_t^n = \begin{cases} \mathbf{0}, & \text{if } v_t^n < 0.3 \text{ m/s}, \\ v_t^n, w_t^n, & \text{else.} \end{cases} \quad (23)$$

Remark 4: We observed that the quadruped robot tended to freeze or become stuck when the commanded linear velocity was below 0.3 m/s, a behavior particularly prevalent on uneven terrain. Additionally, in-place rotation without forward translation occasionally resulted in self-collisions between the robot's legs. To mitigate these issues, we applied a clipping mechanism to the velocity outputs from TRANS-Nav.

B. Network Parameters

The unified networks maintain the same architecture as described in Section V-C, with the only modification being the input shapes for the actor and critic to accommodate the expanded state space. We denote the updated network parameters as ϕ^u , $\psi_{1,2}^u$, $\varphi^{u,a}$, and $\varphi^{u,c}$, which are optimized using the SAC algorithm. To accelerate convergence and enhance performance in complex, uneven environments, we initialize the unified policy by warm-starting these parameters with the weights learned from the original social navigation networks illustrated in Section V.

The first layer of the actor network in the navigation-only policy consists of weights $\mathbf{w}_1^n \in \mathbb{R}^{54 \times 1024}$ and biases $\mathbf{b}_1^n \in \mathbb{R}^{1024}$. In the unified policy, this layer is expanded to accommodate the high-dimensional state space, with weights $\mathbf{w}_1^u \in \mathbb{R}^{118 \times 1024}$ and biases $\mathbf{b}_1^u \in \mathbb{R}^{1024}$. We initialize \mathbf{w}_1^u and \mathbf{b}_1^u based on \mathbf{w}_1^n and \mathbf{b}_1^n as follows:

$$\begin{aligned} \mathbf{w}_1^u[:, 54] &= \mathbf{w}_1^n, \quad \mathbf{w}_1^u[54, :] = \mathbf{0}, \\ \mathbf{b}_1^u[:, 54] &= \mathbf{b}_1^n, \quad \mathbf{b}_1^u[54, :] = \mathbf{0}. \end{aligned} \quad (24)$$

A similar procedure is applied to the first layer of the critic network. Because the remaining layers in the actor, critic, and encoder networks, as detailed in APPENDIX B, share identical dimensions across both the social navigation and unified frameworks, we directly transfer the parameters from the pre-trained social navigation networks to initialize the unified networks.

Algorithm 3 TRANS

- 1: Pre-train locomotion networks with **Algorithm 1**
- 2: Pre-train social navigation networks with **Algorithm 2**
- 3: Expand the social navigation networks according to the extended states $\mathbf{s}_t^{u,*}$
- 4: Freeze the locomotion networks and embed them into the expanded networks
- 5: Initialize the parameters of the unified networks with the updated parameters from social navigation networks
- 6: Update the parameters using the same procedures illustrated in **Algorithm 2**

Finally, the unified pipeline, TRANS, is summarized in **Algorithm 3**.

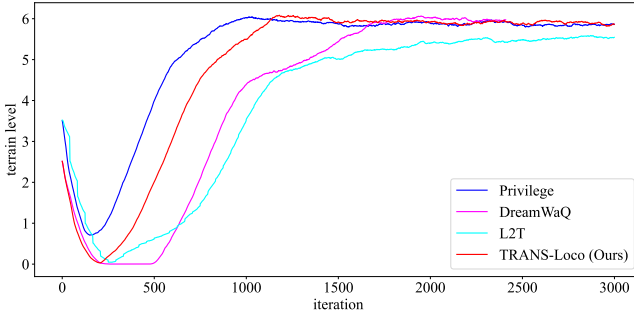


Fig. 6. Progression of terrain difficulty levels over training iterations. The Privilege method yields an ideal performance reference (upper bound) rather than a direct baseline.

VII. SIMULATION EVALUATIONS FOR LOCOMOTION

A. Benchmarks

For a comprehensive evaluation, we compared the following SOTA algorithms:

1) **Privilege** [45]: The actor and critic networks have full access to privileged terrain information, representing the upper-bound performance of the policy.

2) **DreamWaQ** [53]: Our framework builds upon DreamWaQ, utilizing an asymmetric actor-critic DRL architecture.

3) **SLR** [54]: This policy utilizes a symmetric actor-critic DRL architecture, where an encoder extracts latent features shared by both the actor and the critic networks.

4) **L2T** [51]: This method follows a teacher-student paradigm, where the teacher policy first learns quadrupedal locomotion using full access to privileged information. Subsequently, the student policy is trained to clone the teacher's behaviors using only proprioceptive observations available during deployment.

5) **TRANS-Loco**: The proposed method.

Remark 5: Intuitively, the Privilege method adapts efficiently to difficult environments because its locomotion policy explicitly leverages ground-truth terrain data. Consequently, we employ this method exclusively as an ideal performance reference (upper bound) rather than a direct baseline for comparison with sensor-limited methods.

Each of the aforementioned methods was trained using the identical curriculum strategy and domain randomization techniques detailed in Section IV. While DreamWaQ retained its original reward configurations, the other approaches utilized the reward structure defined in TABLE I. All training procedures and experiments were conducted using the Unitree Go2 quadruped platform.

Since the focus of our evaluation is terrain-aware locomotion, we utilize the achieved terrain level as the primary performance metric. The training progression is illustrated in Fig. 6 for a maximum of 3,000 iterations. Notably, SLR was excluded from the figure as it failed around 100 iterations due to early termination triggered by gradient explosion. A similar instability occurred for DreamWaQ around 2,400 iterations. However, when we replaced the standard MLPs in SLR with our CNN-based encoder, the gradient explosion

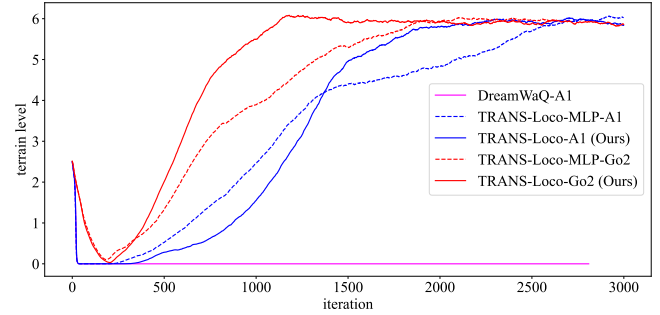


Fig. 7. Ablation analysis of locomotion performance across different hardware platforms and the impact of the modified encoder architecture.

was eliminated, suggesting that our architecture provides superior stability for gradient propagation. Despite this structural improvement, the modified SLR ultimately failed to learn effective locomotion, converging to a zero terrain level, and was therefore also omitted from the final comparison.

Beyond stabilizing gradients, our framework significantly enhances learning efficiency compared to other methods that lack explicit terrain and contact data, such as L2T and the original DreamWaQ. Notably, our approach achieves a learning efficiency comparable to the Privilege method, which has full access to ground-truth data. This performance parity suggests that our architecture effectively extracts and utilizes implicit terrain features from proprioceptive history.

B. Ablations

To verify the performance improvements of our framework, which builds upon DreamWaQ [53], we conducted the following ablation studies:

TRANS-Loco-MLP-Go2: To isolate the impact of our network architecture, we replaced our CNN-based encoder with the MLP architecture from the original DreamWaQ. This variant maintained the Unitree Go2 platform and the fine-tuned reward structure defined in TABLE I.

Cross-embodiment (Unitree A1): We evaluated the portability of our method by replacing the robot platform with the Unitree A1. This set of experiments included:

- **TRANS-Loco-A1:** Our proposed framework deployed on A1.
- **DreamWaQ-A1:** The original DreamWaQ method adapted for A1.
- **TRANS-Loco-MLP-A1:** Our framework using DreamWaQ's MLP-based encoder on A1.

As illustrated in Fig. 7, the DreamWaQ-A1 variant failed to progress, with its terrain level converging to zero during training. In contrast, our proposed TRANS-Loco-A1 framework achieved a high terrain level of 6 on both the A1 and Go2 platforms. This performance gap demonstrates that our modifications to the original DreamWaQ architecture significantly enhance cross-platform generalizability.

Furthermore, the results for TRANS-Loco-MLP-A1 highlight that our fine-tuned reward structure plays a critical role in stabilizing training for the A1 platform. The integration of the CNN-based encoder further accelerated learning efficiency

TABLE III
COMMAND TRACKING ERRORS FOR QUADRUPEDAL LOCOMOTION ON UNEVEN TERRAINS.

Method	Δv_x m/s	Δv_y m/s	Δw_z rad/s
DreamWaQ-Go2	0.12±0.15	0.12±0.15	0.15±0.15
L2T-Go2	0.17±0.18	0.17±0.17	0.28±0.28
TRANS-Loco-MLP-Go2	0.13±0.15	0.12±0.14	0.16±0.17
TRANS-Loco-Go2 (Ours)	0.10±0.12	0.11±0.13	0.13±0.12
TRANS-Loco-MLP-A1	0.16±0.20	0.14±0.17	0.21±0.22
TRANS-Loco-A1 (Ours)	0.14±0.15	0.12±0.13	0.15±0.14

across both quadrupedal platforms, as evidenced by the performance gains in the comparison groups (TRANS-Loco-MLP-Go2 vs. TRANS-Loco-Go2 and TRANS-Loco-MLP-A1 vs. TRANS-Loco-A1).

C. Command Tracking

Since our unified framework relies on high-fidelity velocity tracking during the initial training phase, we further evaluated the command tracking error of our framework against the established benchmarks and ablation models. We randomly distributed 512 robots in simulation and executed 2,000 control steps for each, generating a total of 1,024,000 (1M+) data points for quantitative analysis.

We calculated the mean and standard deviation for the tracking errors across linear xy velocities (Δv_x , Δv_y) and angular z velocity (Δw_z). The results, summarized in TABLE III, demonstrate that our framework (trained on the Go2) achieved the highest tracking accuracy and stability among all non-privileged methods. Furthermore, replacing our CNN-based encoder with an MLP-based architecture resulted in performance degradation for both the Go2 and A1 robots, confirming that our encoder can enhance tracking precision.

To evaluate real-time performance, we selected a representative velocity tracking sequence and compared our framework against the original DreamWaQ on the Go2 platform, as our locomotion controller builds upon its architecture. The tracking performance and corresponding simulation scenes are illustrated in Fig. 8.

During the evaluation, we observed that DreamWaQ resulted in a lower body clearance; the hind legs tended to splay outward and forward, causing hazardous leg-to-obstacle contact rather than proper foot-end interaction. In contrast, while our approach also encountered occasional tripping from obstacles, the policy demonstrated superior adaptability by quickly repositioning the legs and returning to the commanded velocities. DreamWaQ exhibited a significantly slower recovery after stumbling, further validating the enhanced robustness and velocity tracking performance of our framework.

VIII. SIMULATION EVALUATIONS FOR NAVIGATION

A. Benchmarks

To provide a rigorous evaluation of our navigation pipeline, we compare it against a diverse set of benchmarks, including classical geometric planners, optimization-based methods, and DRL approaches:

1) **DWA** [12]: A classical local planner that samples a discrete velocity space and selects the optimal command based on collision avoidance and goal-reaching criteria.

2) **ORCA** [16]: A formal geometric approach that guarantees collision-free motion by assuming reciprocal responsibility among all agents.

3) **AVOCADO** [19]: An advancement over ORCA that treats navigation as an adaptive control problem, allowing the robot to adjust to varying levels of cooperation from other agents in real-time.

4) **N-MPC**: A nonlinear Model Predictive Control strategy that optimizes ego-agent actions over a receding horizon, assuming pedestrians maintain constant velocity.

5) **NeuPAN** [22]: A hybrid method that pre-trains a prediction model to map raw point clouds into a latent distance feature space, which is then utilized by an MPC-based planner for trajectory generation.

6) **T-MPC** [21]: A framework that integrates a global planner to identify topologically distinct navigation paths, which serve as constraints for a local MPC solver.

7) **RGL** [27]: A DRL-based policy that utilizes a Relational Graph Learning architecture, operating under the assumption of perfect state information for all pedestrians.

8) **LNDNL** [29]: A fully end-to-end DRL approach that directly maps raw sensor observations to ego-actions without relying on explicit pedestrian state estimation.

9) **DRL-VO** [35]: A hybrid policy leveraging both pedestrian states and raw observations. To ensure a fair comparison, we integrated the Encoder-integrated SAC structure described in Section V to address original training instabilities.

10) **TRANS-Nav**: The proposed method.

To ensure a fair and consistent evaluation, we standardized the environmental dynamics and agent constraints across all compared methods. We utilized ORCA to simulate deterministic pedestrian motions, intentionally omitting stochastic noise to isolate the performance of the navigation policies. Furthermore, we synchronized the kinematic limits of the ego-agent across all baselines, applying the same linear and angular velocity constraints used in our proposed framework.

Learning performance. We first evaluated our learning framework against existing DRL-based approaches, with the results illustrated in Fig. 9. We terminated the training of RGL prematurely as its success rate remained significantly lower than other methods; furthermore, its computational overhead was over 15 times that of our approach due to the exhaustive traversal of its discrete action space.

Both RGL and LNDNL converged to suboptimal success rates when subjected to the ego-agent's velocity constraints, suggesting that our social navigation framework is more robust under strict kinematic limitations. While DRL-VO achieved a comparable learning efficiency, it did so only after being integrated with our proposed network structure, further validating the effectiveness and stability of our architectural design.

Quantitative analysis. To ensure statistical reliability, we conducted 500 evaluation trials for each method, ensuring that initial environmental configurations were identical across all test cases. Navigation performance was quantified using the following metrics:

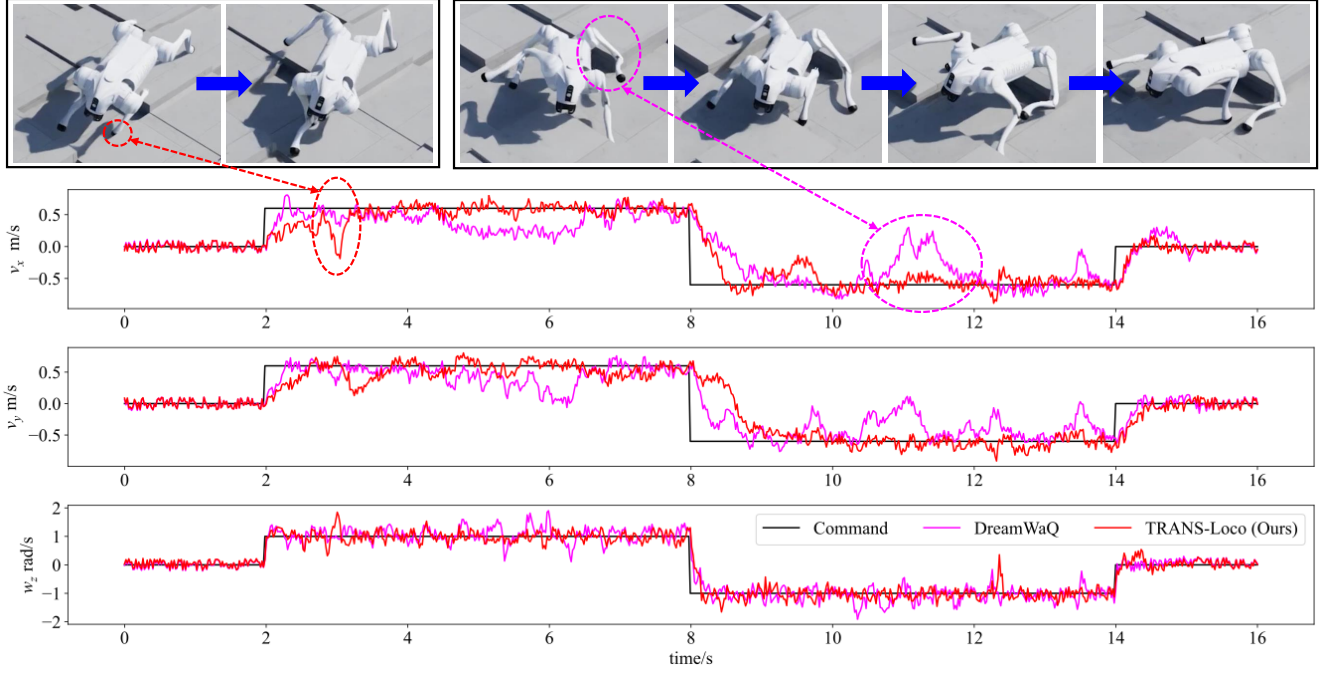


Fig. 8. Velocity tracking performance along with simulation scenes. The commanded velocities, $[v_x, v_y, v_z]$, change from $[0.0, 0.0, 0.0]$, to $[0.6, 0.6, 1.0]$, to $[-0.6, -0.6, -1.0]$, and to $[0.0, 0.0, 0.0]$. The top left two scenes correspond to the peak tracking errors for our approach, and the other four illustrate the erroneous tracking for DreamWaQ.

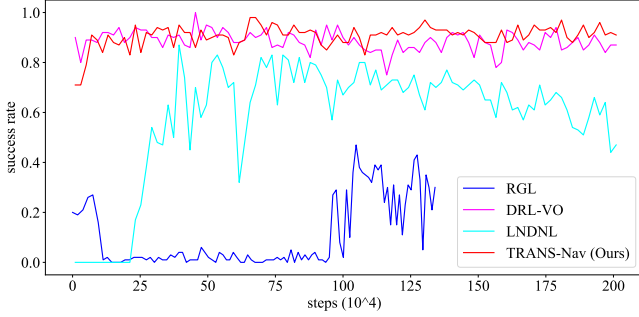


Fig. 9. Learning efficiency comparison. DRL-VO achieves comparable efficiency to our method when utilizing our proposed network architecture.

Success Rate (SR): Percentage of trials where the agent reached the goal safely.

Collision Rate (CR): Percentage of trials resulting in contact with obstacles or pedestrians.

Timeout Rate (TR): Percentage of trials where the agent failed to reach the goal within the allocated time limit.

Average Navigation Time (NT): The mean time taken to reach the goal, calculated exclusively for successful trials to avoid skewing data with failed attempts.

Compared to the DRL-based baselines, RGL, LNDNL, and DRL-VO, our framework demonstrated superior performance as evidenced by a higher Success SR, a lower CR, and a zero TR, as shown in TABLE IV. Although RGL exhibited a shorter NT, our analysis indicates this was due to a reckless policy that prioritized a direct trajectory toward the goal while neglecting necessary collision avoidance. While the original RGL can achieve a comparable SR in unconstrained environments, its

TABLE IV
NAVIGATION EVALUATIONS WITH 500 RANDOM TESTS.

	Method	SR	CR	TR	NT
Reactive	DWA	0.946	0.014	0.040	18.81 ± 3.36
	ORCA	0.848	0.004	0.148	20.33 ± 5.59
	AVOCADO	0.830	0.044	0.126	18.56 ± 4.61
MPC	N-MPC	0.242	0.002	0.756	19.89 ± 3.85
	NeuPAN	0.004	0.020	0.976	40.20 ± 0.85
	T-MPC	0.326	0.586	0.106	19.50 ± 7.31
DRL	RGL	0.326	0.494	0.180	16.88 ± 0.40
	LNDNL	0.926	0.022	0.052	27.88 ± 6.13
	DRL-VO	0.928	0.072	0.000	19.06 ± 1.92
TRANS-Nav (Ours)		0.972	0.028	0.000	19.26 ± 1.29

performance significantly degrades under our specific testing conditions, highlighting our framework's superior ability to maintain safety and efficiency under strict action and velocity limitations.

In addition to DRL-based methods, we compared our framework against MPC-based trajectory optimization approaches, including N-MPC, T-MPC, and NeuPAN, as summarized in TABLE IV. Both N-MPC and NeuPAN frequently exhibited the “frozen robot” problem, as their conservative motion planners failed to find feasible solutions within socially interactive scenarios. Conversely, while T-MPC avoided overly conservative behavior, its inherent aggressiveness led to a higher frequency of collisions. A primary factor in the failure of these MPC-based approaches was the application of stricter velocity constraints, which limited the available solution space and necessitated extensive parameter fine-tuning. Similarly, these

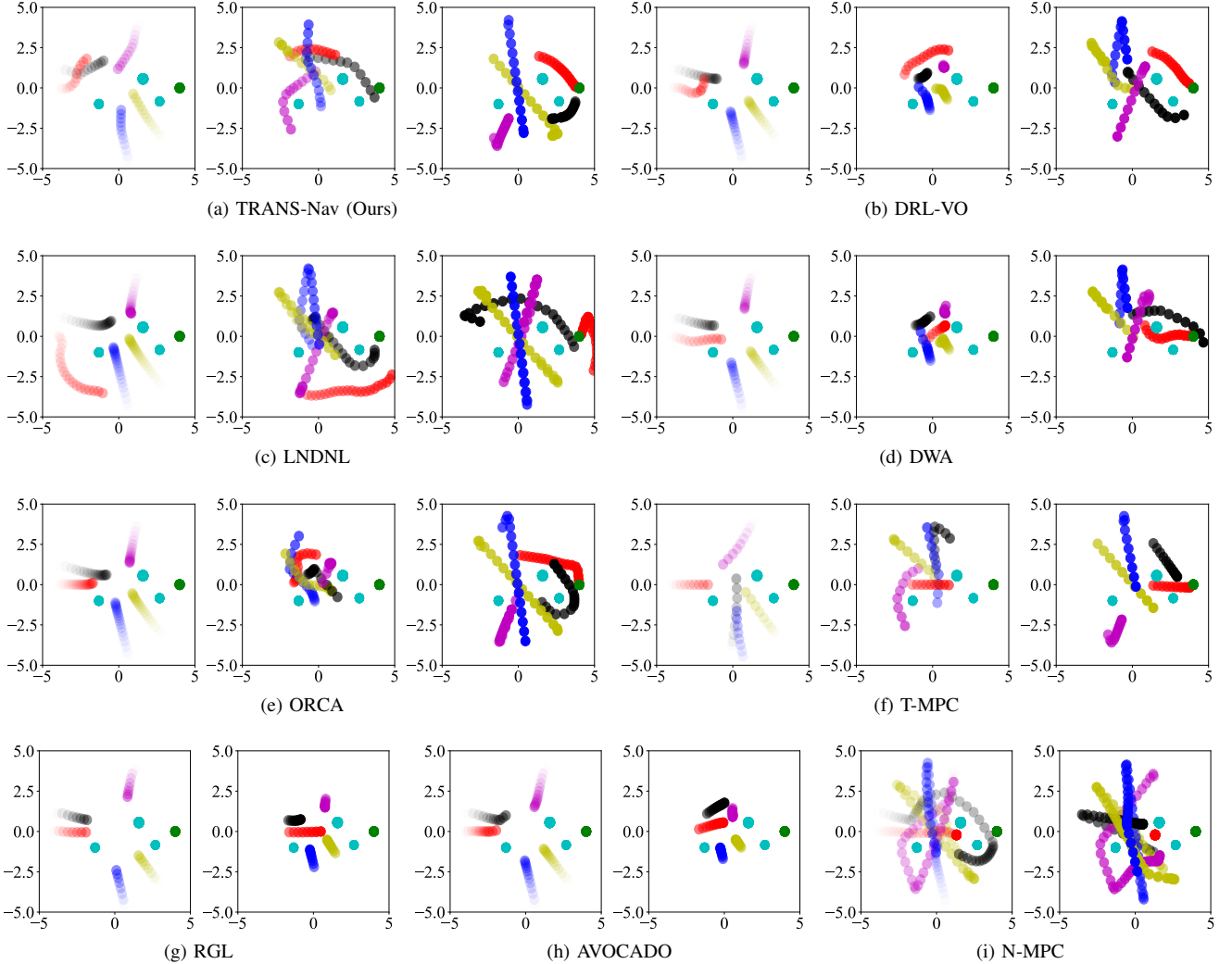


Fig. 10. Trajectories of the ego-agent and pedestrians. The red circle is the ego-agent, the green represents the goal, the cyan circles are static obstacles, and others are pedestrians. As time goes by, the color of the circle changes from light to dark. TRANS-Nav, DRL-VO, LNDNL, DWA, ORCA, and T-MPC succeeded in reaching the goal without collision, so we separately plotted three sub-figures. Relatively, two adjacent sub-figures were provided for other failure methods, including RGL, AVOCADO, and N-MPC.

kinematic constraints degraded the performance of geometric methods such as DWA, ORCA, and AVOCADO, further demonstrating our framework’s superior adaptability to highly constrained action spaces.

Trajectory of ego-agent. To evaluate the behavioral characteristics of each method, we analyzed a representative scenario featuring three static obstacles and four dynamic pedestrians. The resulting trajectories are visualized in Fig. 10, revealing distinct navigation strategies:

- **Aggressive and reckless:** As shown in Fig. 10(g), RGL prioritized goal-reaching speed over safety, often failing to maintain adequate clearance for collision avoidance.
- **Conservative and frozen:** N-MPC frequently suffered from “frozen motion” due to its conservative optimization constraints (Fig. 10(i), right), while LNDNL maintained excessively large safety margins (Fig. 10(c)), significantly prolonging travel time.
- **High-risk proximity:** T-MPC was less conservative but navigated dangerously close to obstacles (see Fig. 10(f)),

leading to the high failure rates noted in TABLE IV. Similarly, DWA often steered the agent into “discomfort zones” near obstacles (see Fig. 10(d)), increasing collision risks.

- **Interaction bottlenecks:** ORCA trajectories (see Fig. 10(e)) exhibited significant deceleration during multi-pedestrian interactions. While AVOCADO (see Fig. 10(h)) mitigated this slowdown, it did so at the expense of safety.
- **Optimal balance:** Our framework and the modified DRL-VO produced nearly identical, efficient trajectories, as shown in Fig. 10(a) and (b). This convergence further underscores the effectiveness of our network architecture in balancing safety, speed, and constraint satisfaction.

B. Ablations

To evaluate the effectiveness of our social navigation pipeline, we conducted the following ablation studies:

TABLE V
TRANS-NAV: ABLATION EVALUATIONS WITH 500 RANDOM TESTS.

Method	SR	CR	NT
TRANS-Nav-CNN	0.892	0.108	18.96±1.40
TRANS-Nav-Direct	0.956	0.064	20.66±2.83
TRANS-Nav-Noise	0.960	0.040	18.75±1.48
TRANS-Nav (Ours)	0.972	0.028	19.26±1.29

1) **TRANS-Nav-PPO**: We replaced the SAC algorithm with PPO to test the impact of the RL framework. However, the success rate remained at zero throughout the training phase, leading us to exclude this variant from further analysis.

2) **TRANS-Nav-CNN**: We enabled CNN updates in both the actor and critic networks to empirically verify the stability and performance claims made in *Remark 3*.

3) **TRANS-Nav-Direct**: To assess the impact of our proposed LiDAR scan transformation, we implemented a version that utilizes direct, raw LiDAR scans. This allows us to isolate the benefits of our spatial data processing.

4) **TRANS-Nav-Noise**: While our initial comparisons against model-based and DRL-based methods were conducted in noise-free environments for maximum control, we implemented this variant using the domain randomization described in Section V-F. This demonstrates the framework’s robustness and its readiness for sim-to-real transfer.

Our analysis revealed that while TRANS-Nav-Direct and TRANS-Nav-Noise followed training trajectories similar to the original framework, TRANS-Nav-CNN suffered from significantly degraded learning performance. The quantitative results of these 500 evaluations are summarized in TABLE V.

Notably, our framework maintained a performance level that outperformed the baselines from TABLE IV even when subjected to noise, underscoring its robustness and potential for sim-to-real transfer. In the TRANS-Nav-Direct study, the use of raw LiDAR scans without transformation led to a marked decrease in success rate and increase in navigation time; this confirms that our proposed LiDAR transformation more effectively captures the complex dynamics and interactions between the robot and its environment. Finally, enabling CNN updates in both the actor and critic networks resulted in a substantial performance drop, empirically validating the architectural advantages detailed in *Remark 3*.

IX. SIMULATION EVALUATIONS FOR UNIFIED POLICY

A. Ablations

To verify the performance improvements provided by our unified policy, we conducted the following ablation studies:

1) **Nav-Loco**: We decoupled the navigation planner from the locomotion controller. In this setup, the navigation policy first generates a commanded CoM velocity without considering full-body quadrupedal dynamics. These commands are then tracked by our locomotion controller on uneven terrain. This study isolates the benefits of our unified architecture over a traditional hierarchical approach.

2) **Train-Nav-Loco**: We retrained TRANS-Nav without the low-level states $\{\hat{v}_t, z_t^l, o_t^l\}$ and omitted the action clipping

TABLE VI
TRANS: ABLATION EVALUATIONS WITH 500 RANDOM TESTS.

Method	SR	CR	TR	NT
Nav-Loco	0.924	0.076	0.000	19.62±2.20
Train-Nav-Loco	0.930	0.066	0.004	19.54±2.26
TRANS-Direct	0.924	0.076	0.000	19.60±2.15
TRANS-Warm-Start	0.954	0.042	0.004	20.39±2.81
TRANS-Clip	0.916	0.076	0.008	21.28±3.38
TRANS (Ours)	0.976	0.024	0.000	20.57±3.68

defined in Eq. (23). Concurrently, the navigation policy was initialized using a warm-start from the original TRANS-Nav, while the locomotion controller remained frozen.

3) **TRANS-Direct**: We retrained the TRANS framework from scratch using random parameter initialization, omitting both the warm-start phase and action clipping. The target linear velocity v_t^n was sampled continuously from 0.0 to 0.5 m/s.

4) **TRANS-Warm-Start**: The network parameters were initialized using the warm-start procedure defined in Eq. (24), but no action clipping was applied to the output.

5) **TRANS-Clip**: We implemented the action clipping strategy defined in Eq. (23) while exempting the network from the warm-start initialization.

The final quantitative evaluation across 500 randomized trials is summarized in TABLE VI. Our results indicate that the traditional decoupled pipeline, Nav-Loco, suffers from a reduced success rate due to the gap between high-level planning and low-level execution. Retraining the unified policy from scratch (TRANS-Direct) yielded performance comparable to the decoupled baseline, suggesting that naive learning alone is insufficient without proper guidance.

However, applying warm-start initialization increased the success rate by 3%, confirming that pre-training with TRANS-Nav effectively bootstraps quadrupedal social navigation on uneven terrains. Furthermore, TRANS-Warm-Start achieved a superior success rate compared to Train-Nav-Loco (0.954 vs. 0.930), suggesting that the incorporation of low-level states enhances quadrupedal social navigation across uneven terrains.

While individual action clipping slightly degraded performance in simulation, it remains a vital component for ensuring safe sim-to-real transfer. Notably, the synergy between warm-start initialization and action clipping significantly boosted the success rate to 0.976, surpassing even the standalone TRANS-Nav. This peak performance highlights our architecture’s exceptional adaptability to the discrete and highly constrained action spaces inherent in legged robot navigation.

B. Failure Analysis

Despite the unified policy achieving a high success rate (0.976), infrequent failures were still recorded. As illustrated in Fig. 11, we categorized the observed collisions into three distinct failure modes: head-on collisions, pedestrian rear-end collisions, and robot rear-end collisions. Out of 500 trials reported in TABLE VI, 12 collisions occurred: 3 head-on, 3 robot rear-end, and 6 pedestrian rear-end. Failure analysis is given as follows:

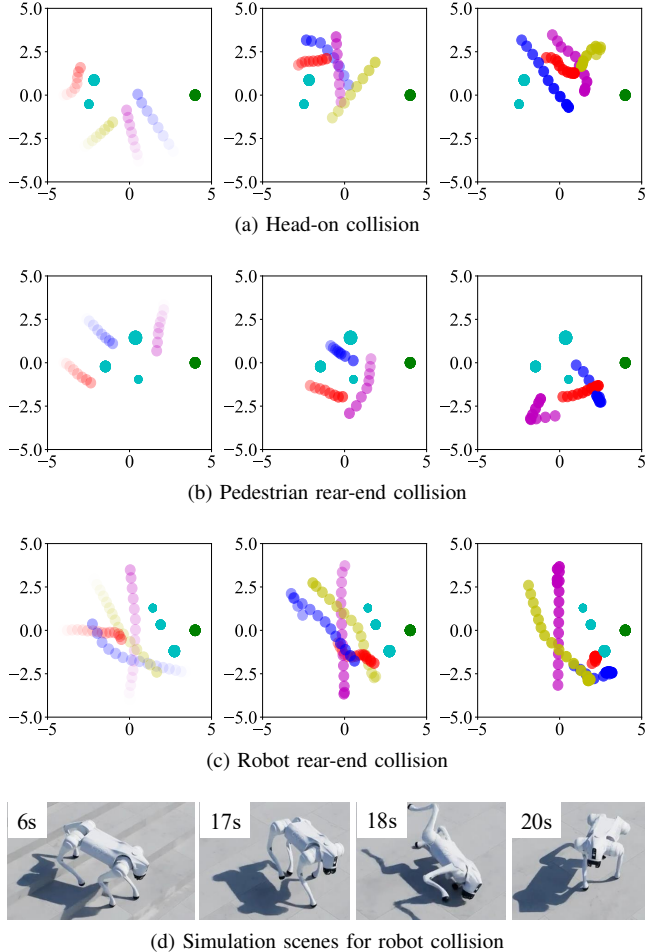


Fig. 11. Trajectories and simulation environments for representative failure cases. (a) Top row: A head-on collision between the robot and a dynamic pedestrian. (b) Middle row: A scenario where a pedestrian rear-ends the robot due to reactivity differences. (c) Third row: Trajectory analysis of a collision with a static obstacle. (d) Bottom row: Corresponding 3D simulation snapshots for the obstacle collision cases presented in (c).

Pedestrian dynamics: Because the pedestrian motion generator is highly reactive while the robot is governed by strict velocity constraints, pedestrians are statistically more likely to rear-end the robot.

Mutual avoidance errors: Despite reciprocal avoidance efforts from both parties, head-on collisions occasionally persist. A potential mitigation strategy involves adopting more conservative behaviors, such as a “temporary stop” command upon predicting a high-risk interaction.

Terrain and maneuverability: We observed occasional robot drift caused by challenging terrain, leading to rear-end collisions with pedestrians. Furthermore, the robot occasionally became “stuck” near static obstacles. While rotating in place offers a recovery path, it can induce locomotion instability and inadvertently trigger rear-end contact.

To address these limitations, we will focus on:

Enhanced rotational stability: Improving the stability of high-torque rotational maneuvers for quadruped robots on uneven terrain.

Recovery behaviors: Enabling safe backward locomotion to recover from stalled or “frozen” states without compromis-

TABLE VII
HARDWARE IMPLEMENTATIONS.

Scenarios/Counts	flat	uneven	slopes	stairs
Success/Failure	3/0	4/1	3/0	6/4

ing full-body balance.

X. HARDWARE IMPLEMENTATIONS

A. Quadruped Navigation System

The hardware configuration and computational workflow for our deployment are illustrated in Fig. 12. We utilize a Unitree Go2 quadrupedal robot equipped with a Livox MID-360 LiDAR and a ZED2 stereo camera. The software architecture is executed on an external laptop (Intel i7-10750H CPU, NVIDIA GTX 1650 Ti GPU) and is comprised of the following functional modules:

- **LiDAR-IMU:** Manages raw data acquisition from the LiDAR and IMU sensors, ensuring precise time synchronization before data publishing.
- **SLAM-Loc:** Subscribes to synchronized LiDAR and IMU streams and employs the FAST-LIO algorithm to provide high-frequency global localization.
- **Human-Pos:** Processes stereo camera data via the ZED2 SDK to detect pedestrians and estimate their spatial coordinates within the camera frame.
- **LiDAR-Trans:** Integrates global localization and human position data to reconstruct and transform historical LiDAR scans. It computes the latent features \mathbf{z}_t^n and determines the goal position \mathbf{g}_t relative to the robot frame.
- **Quad-Loco:** Executes the TRANS-Loco controller to handle full-body locomotion. It subscribes to velocity commands from the high-level navigation planner and publishes the estimated velocity $\hat{\mathbf{v}}_t$, latent locomotion features \mathbf{z}_t^l , and proprioceptive observations \mathbf{o}_t^l .
- **Vel-Cmd:** Acts as the high-level decision maker, subscribing to all state features, $[\mathbf{z}_t^n, \mathbf{g}_t, \hat{\mathbf{v}}_t, \mathbf{z}_t^l, \mathbf{o}_t^l]$, to generate the final velocity commands.

To manage inter-module communication and data synchronization, we utilize ROS Noetic with a multi-rate execution strategy: the IMU publishes at 200Hz, Quad-Loco operates at 50Hz, SLAM-Loc and Human-Pos are synchronized at 10Hz, and the high-level LiDAR-Trans and Vel-Cmd modules run at 5Hz. To eliminate computational resource competition, we implemented a dedicated CPU affinity strategy across 12 cores, allocating 4 cores to the computationally intensive LiDAR-Trans module and the remainder distributed among sensing and control tasks. Under full system load, the execution latencies for SLAM-Loc, Human-Pos, LiDAR-Trans, Quad-Loco, and Vel-Cmd were recorded at 2.5, 28.5, 7.6, 1.7, and 0.8 ms, respectively. These results confirm the real-time feasibility of our framework, as the critical control and planning modules operate well within their respective timing budgets.

B. Real-world Implementations

We evaluated our policy across a diverse range of environments, including indoor flat and uneven surfaces, outdoor

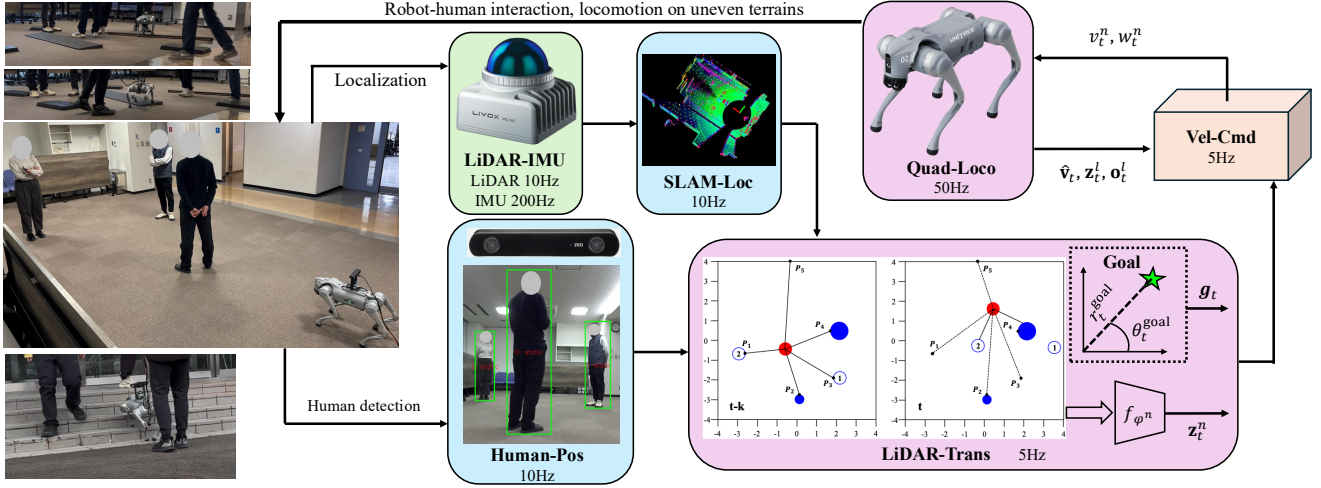


Fig. 12. Overview of the hardware deployment pipeline. Visual data for pedestrian tracking is acquired via the onboard camera, while localized navigation is achieved through LiDAR-IMU fusion. These data streams are processed on an external PC to execute the real-time perception-to-action mapping.



Fig. 13. Representative hardware trajectories and scenes. Each column depicts a full navigation trial. The composite plots overlay real-time localization, pedestrian tracking, and LiDAR reconstruction data onto the physical environment.

cement and grass slopes, and stairs with a 12 cm step height. The quantitative success rates are summarized in TABLE

VII, while the supplementary videos provide a qualitative demonstration of the system's real-world performance.

The majority of failures were observed during stair traversal, indicating that the simultaneous demand for collision avoidance and stair climbing remains a significant sim-to-real challenge. Furthermore, a recurring challenge observed across all experimental scenarios was localization drift, primarily induced by high-frequency structural vibrations and the presence of dynamic environmental features. These factors significantly degraded real-world performance; consequently, our future research will prioritize the enhancement of localization stability through robust state estimation techniques. Two representative hardware deployments and the corresponding robot and pedestrian trajectories are illustrated in Fig. 13.

XI. DISCUSSIONS

While our extensive simulation benchmarks and ablation studies demonstrate the framework's effectiveness, several sim-to-real discrepancies remain. Stair environments proved particularly challenging, as the simultaneous demand for balancing and dynamic obstacle avoidance pushed the policy to its limits. Furthermore, despite fusing IMU data, we observed that high-frequency vibrations from quadrupedal locomotion often induced localization drift in the LiDAR SLAM algorithm, degrading real-world navigation accuracy. Another critical hardware constraint is the limited Field of View (FoV) of the onboard camera; unlike the 360° FoV available in simulation, our hardware deployment assumes pedestrians outside the camera's range will actively avoid the robot. Addressing these sensing and environmental gaps is a primary objective for future development.

The modeling of human behavior presents an additional limitation. While we utilize ORCA to simulate multi-agent interactions, which is consistent with established literature, this model does not fully capture the complexity and diversity of real-world human interactions. Such discrepancies can impede the transferability of the navigation policy from virtual environments to real-world spaces. Consequently, future research will focus on integrating more sophisticated and heterogeneous interaction models into our simulation pipeline to enhance the robustness and reliability during practical deployment.

XII. CONCLUSIONS

In this work, we presented a unified social navigation policy for quadruped robots operating on uneven terrains. Our framework employs a two-stage training strategy: first, we independently developed a high-level motion planning policy for socially interactive environments using a differential-drive kinematic model and a low-level locomotion controller tailored to specific quadrupedal dynamics. In the second stage, these components were integrated into a single, socially aware policy capable of simultaneously managing complex pedestrian interactions and uneven terrain traversal.

Comprehensive benchmarks and ablation studies validated the effectiveness of the proposed architecture, while extensive real-world deployments demonstrated its robust sim-to-real transfer potential across diverse environments. To address current limitations, future work will focus on enhancing locomotion stability, specifically for challenging tasks like

TABLE VIII
LOCOMOTION NETWORKS: ACTOR, CRITIC, AND DECODER

Networks	Input shape	Hidden layers	Output shape
Actor	(64,)	$512 \times 256 \times 128$	(12,)
Critic	(286,)	$512 \times 256 \times 128$	(1,)
Decoder	(19,)	64×128	(45,)

TABLE IX
LOCOMOTION NETWORKS: ENCODER

Layer	Operation
1	Conv2d(1, 16, kernel_size=3, stride=1, padding=1)
2	MaxPool2d(kernel_size=2, stride=2, padding=0)
3	Conv2d(16, 32, kernel_size=3, stride=1, padding=1)
4	MaxPool2d(kernel_size=2, stride=2, padding=0)
5	Conv2d(32, 64, kernel_size=3, stride=1, padding=1)
6	Flatten with output shape (1408,)
7	Linear(1408, 64)
Output	$2 \times \text{Linear}(64, 3), 2 \times \text{Linear}(64, 16)$

TABLE X
SOCIAL NAVIGATION NETWORKS: ACTOR, CRITIC, AND DECODER

Networks	Input shape	Hidden layers	Output shape
Actor	(54)	1024×1024	(4,)
Critic	(56,)	1024×1024	(1,)

TABLE XI
SOCIAL NAVIGATION NETWORKS: ENCODER

Layer	Operation
1	Conv2d(1, 32, kernel_size=(2, 20), stride=(1, 10))
2	MaxPool2d(kernel_size=(1, 5))
3	Conv2d(32, 32, kernel_size=2, stride=1)
4	MaxPool2d(kernel_size=(1, 2))
5	Flatten with output shape (2176,)
6	Linear(2176, 1024)
Output	(50,)

stair traversal. Additionally, we aim to improve the realism of our simulation environments by integrating diverse and heterogeneous pedestrian interaction models to broadly reflect the complexity of real-world human behavior.

APPENDIX

A. Locomotion Networks

TABLES VIII and IX detail the locomotion networks.

B. Navigation Networks

TABLES X and XI detail the locomotion networks.

REFERENCES

[1] S. Ha, J. Lee, M. Panne, Z. Xie, W. Yu, and M. Khadiv, "Learning-based legged locomotion: State of the art and future perspectives," *The International Journal of Robotics Research*, vol. 44, no. 8, pp. 1396–1427, 2025.

[2] H. Xie, C. Cui, X. Zhong, X. Zhong, and Q. Liu, "Real-time support terrain mapping and terrain adaptive local planning for quadruped robots," *IEEE Robotics and Automation Letters*, vol. 9, no. 12, pp. 11 018–11 025, 2024.

[3] C. Zhang, J. Jin, J. Frey, N. Rudin, M. Mattamala *et al.*, "Resilient legged local navigation: Learning to traverse with compromised perception end-to-end," in *IEEE International Conference on Robotics and Automation (ICRA)*, 2024, pp. 34–41.

[4] A. Francis, A. Faust, H.-T. L. Chiang, J. Hsu, J. C. Kew *et al.*, "Long-range indoor navigation with prm-rl," *IEEE Transactions on Robotics*, vol. 36, no. 4, pp. 1115–1134, 2020.

[5] A. Devo, G. Mezzetti, G. Costante, M. L. Fravolini, and P. Valigi, "Towards generalization in target-driven visual navigation by using deep reinforcement learning," *IEEE Transactions on Robotics*, vol. 36, no. 5, pp. 1546–1561, 2020.

[6] T. Duong, M. Yip, and N. Atanasov, "Autonomous navigation in unknown environments with sparse bayesian kernel-based occupancy mapping," *IEEE Transactions on Robotics*, vol. 38, no. 6, pp. 3694–3712, 2022.

[7] W. Xiao, T.-H. Wang, R. Hasani, M. Chahine, A. Amini *et al.*, "Barriernet: Differentiable control barrier functions for learning of safe robot control," *IEEE Transactions on Robotics*, vol. 39, no. 3, pp. 2289–2307, 2023.

[8] P. T. Singamaneni, P. Bachiller-Burgos, L. J. Manso, A. Garrell, A. Sanfeliu *et al.*, "A survey on socially aware robot navigation: Taxonomy and future challenges," *The International Journal of Robotics Research*, vol. 43, no. 10, pp. 1533–1572, 2024.

[9] A. Alahi, K. Goel, V. Ramanathan, A. Robicquet, L. Fei-Fei, and S. Savarese, "Social lstm: Human trajectory prediction in crowded spaces," in *Proceedings of the IEEE conference on computer vision and pattern recognition*, 2016, pp. 961–971.

[10] K. Zhu and T. Zhang, "Deep reinforcement learning based mobile robot navigation: A review," *Tsinghua Science and Technology*, vol. 26, no. 5, pp. 674–691, 2021.

[11] T. Fan, P. Long, W. Liu, and J. Pan, "Distributed multi-robot collision avoidance via deep reinforcement learning for navigation in complex scenarios," *The International Journal of Robotics Research*, vol. 39, no. 7, pp. 856–892, 2020.

[12] D. Fox, W. Burgard, and S. Thrun, "The dynamic window approach to collision avoidance," *IEEE Robotics and Automation Magazine*, vol. 4, no. 1, pp. 23–33, 2002.

[13] M. Dobrevski and D. Skočaj, "Dynamic adaptive dynamic window approach," *IEEE Transactions on Robotics*, vol. 40, pp. 3068–3081, 2024.

[14] D. Helbing and P. Molnar, "Social force model for pedestrian dynamics," *Physical review E*, vol. 51, no. 5, p. 4282, 1995.

[15] G. Ferrer and A. Sanfeliu, "Proactive kinodynamic planning using the extended social force model and human motion prediction in urban environments," in *IEEE/RSJ International Conference on Intelligent Robots and Systems (IROS)*, 2014, pp. 1730–1735.

[16] J. Van Den Berg, S. J. Guy, M. Lin, and D. Manocha, "Reciprocal n-body collision avoidance," in *Robotics Research: The 14th International Symposium*, 2011, pp. 3–19.

[17] J. Alonso-Mora, A. Breitenmoser, M. Rufli, P. Beardsley, and R. Siegwart, "Optimal reciprocal collision avoidance for multiple non-holonomic robots," in *Distributed Autonomous Robotic Systems: The 10th International Symposium*, 2013, pp. 203–216.

[18] K. Guo, D. Wang, T. Fan, and J. Pan, "Vr-orca: Variable responsibility optimal reciprocal collision avoidance," *IEEE Robotics and Automation Letters*, vol. 6, no. 3, pp. 4520–4527, 2021.

[19] D. Martínez-Baselga, E. Sebastián, E. Montijano, L. Riazuelo, C. Sagüés, and L. Montano, "Avocado: Adaptive optimal collision avoidance driven by opinion," *IEEE Transactions on Robotics*, vol. 41, pp. 2495–2511, 2025.

[20] O. de Groot, L. Ferranti, D. M. Gavrila, and J. Alonso-Mora, "Scenario-based motion planning with bounded probability of collision," *The International Journal of Robotics Research*, vol. 44, no. 9, pp. 1507–1525, 2025.

[21] O. De Groot, L. Ferranti, D. M. Gavrila, and J. Alonso-Mora, "Topology-driven parallel trajectory optimization in dynamic environments," *IEEE Transactions on Robotics*, vol. 41, pp. 110–126, 2025.

[22] R. Han, S. Wang, S. Wang, Z. Zhang, J. Chen *et al.*, "Neupan: Direct point robot navigation with end-to-end model-based learning," *IEEE Transactions on Robotics*, vol. 41, pp. 2804–2824, 2025.

[23] Z. Xie and P. Dames, "Scope: Stochastic cartographic occupancy prediction engine for uncertainty-aware dynamic navigation," *IEEE Transactions on Robotics*, vol. 41, pp. 4139–4158, 2025.

[24] H. Thomas, J. Zhang, and T. D. Barfoot, "The foreseeable future: Self-supervised learning to predict dynamic scenes for indoor navigation," *IEEE Transactions on Robotics*, vol. 39, no. 6, pp. 4581–4599, 2023.

[25] Y. F. Chen, M. Liu, M. Everett, and J. P. How, "Decentralized non-communicating multiagent collision avoidance with deep reinforcement learning," in *IEEE International Conference on Robotics and Automation (ICRA)*, 2017, pp. 285–292.

[26] C. Chen, Y. Liu, S. Kreiss, and A. Alahi, "Crowd-robot interaction: Crowd-aware robot navigation with attention-based deep reinforcement learning," in *IEEE International Conference on Robotics and Automation (ICRA)*, 2019, pp. 6015–6022.

[27] C. Chen, S. Hu, P. Nikdel, G. Mori, and M. Savva, "Relational graph learning for crowd navigation," in *IEEE/RSJ International Conference on Intelligent Robots and Systems (IROS)*, 2020, pp. 10 007–10 013.

[28] J. Jin, N. M. Nguyen, N. Sakib, D. Graves, H. Yao, and M. Jagersand, "Mapless navigation among dynamics with social-safety-awareness: A reinforcement learning approach from 2d laser scans," in *IEEE International Conference on Robotics and Automation (ICRA)*, 2020, pp. 6979–6985.

[29] W. Zhu and M. Hayashibe, "Learn to navigate in dynamic environments with normalized lidar scans," in *IEEE International Conference on Robotics and Automation (ICRA)*, 2024, pp. 7568–7575.

[30] G. Monaci, M. Aractingi, and T. Silander, "Dipean: Distilling privileged information for crowd-aware navigation," in *Robotics: Science and Systems (RSS)*, 2022.

[31] W. Zhu and M. Hayashibe, "Autonomous navigation system in pedestrian scenarios using a dreamer-based motion planner," *IEEE Robotics and Automation Letters*, vol. 8, no. 6, pp. 3836–3843, 2023.

[32] H. Yang, C. Yao, C. Liu, and Q. Chen, "Rmrl: Robot navigation in crowd environments with risk map-based deep reinforcement learning," *IEEE Robotics and Automation Letters*, vol. 8, no. 12, pp. 7930–7937, 2023.

[33] A. J. Sathyamoorthy, J. Liang, U. Patel, T. Guan, R. Chandra, and D. Manocha, "Densecavoid: Real-time navigation in dense crowds using anticipatory behaviors," in *IEEE International Conference on Robotics and Automation (ICRA)*, 2020, pp. 11 345–11 352.

[34] S. Yao, G. Chen, Q. Qiu, J. Ma, X. Chen, and J. Ji, "Crowd-aware robot navigation for pedestrians with multiple collision avoidance strategies via map-based deep reinforcement learning," in *IEEE/RSJ International Conference on Intelligent Robots and Systems (IROS)*, 2021, pp. 8144–8150.

[35] Z. Xie and P. Dames, "Drl-vo: Learning to navigate through crowded dynamic scenes using velocity obstacles," *IEEE Transactions on Robotics*, vol. 39, no. 4, pp. 2700–2719, 2023.

[36] L. Qin, Z. Huang, C. Zhang, H. Guo, M. Ang, and D. Rus, "Deep imitation learning for autonomous navigation in dynamic pedestrian environments," in *IEEE International Conference on Robotics and Automation (ICRA)*, 2021, pp. 4108–4115.

[37] H. Karnan, A. Nair, X. Xiao, G. Warnell, S. Pirk *et al.*, "Socially compliant navigation dataset (scand): A large-scale dataset of demonstrations for social navigation," *IEEE Robotics and Automation Letters*, vol. 7, no. 4, pp. 11 807–11 814, 2022.

[38] D. M. Nguyen, M. Nazeri, A. Payandeh, A. Datar, and X. Xiao, "Toward human-like social robot navigation: A large-scale, multi-modal, social human navigation dataset," in *IEEE/RSJ International Conference on Intelligent Robots and Systems (IROS)*, 2023, pp. 7442–7447.

[39] V.-A. Le, B. Chalaki, V. Tadiparthi, H. N. Mahjoub, J. D'sa, and E. Moradi-Pari, "Social navigation in crowded environments with model predictive control and deep learning-based human trajectory prediction," in *IEEE/RSJ International Conference on Intelligent Robots and Systems (IROS)*, 2024, pp. 4793–4799.

[40] S. Park, M. Cap, J. Alonso-Mora, C. Ratti, and D. Rus, "Social trajectory planning for urban autonomous surface vessels," *IEEE Transactions on Robotics*, vol. 37, no. 2, pp. 452–465, 2020.

[41] P. Wang, D. Liu, J. Chen, H. Li, and C.-Y. Chan, "Decision making for autonomous driving via augmented adversarial inverse reinforcement learning," in *IEEE International Conference on Robotics and Automation (ICRA)*, 2021, pp. 1036–1042.

[42] T. Phan-Minh, F. Howington, T.-S. Chu, M. S. Tomov, R. E. Beaudoin *et al.*, "Driveirl: Drive in real life with inverse reinforcement learning," in *IEEE International Conference on Robotics and Automation (ICRA)*, 2023, pp. 1544–1550.

[43] A. Agrawal, S. Chen, A. Rai, and K. Sreenath, "Vision-aided dynamic quadrupedal locomotion on discrete terrain using motion libraries," in *IEEE International Conference on Robotics and Automation (ICRA)*, 2022, pp. 4708–4714.

[44] T. Miki, L. Wellhausen, R. Grandia, F. Jenelten, T. Homberger, and M. Hutter, “Elevation mapping for locomotion and navigation using gpu,” in *IEEE/RSJ International Conference on Intelligent Robots and Systems (IROS)*, 2022, pp. 2273–2280.

[45] T. Miki, J. Lee, J. Hwangbo, L. Wellhausen, V. Koltun, and M. Hutter, “Learning robust perceptive locomotion for quadrupedal robots in the wild,” *Science Robotics*, vol. 7, no. 62, p. eabk2822, 2022.

[46] I. T. Kurniawan, W. Zhu, D. Owaki, and M. Hayashibe, “Learning perceptive legged robot locomotion in the real world: A systematic review,” *IEEE Robotics and Automation Magazine*, pp. 2–18, 2025.

[47] Y. Kim, H. Oh, J. Lee, J. Choi, G. Ji *et al.*, “Not only rewards but also constraints: Applications on legged robot locomotion,” *IEEE Transactions on Robotics*, vol. 40, pp. 2984–3003, 2024.

[48] J. Lee, J. Hwangbo, L. Wellhausen, V. Koltun, and M. Hutter, “Learning quadrupedal locomotion over challenging terrain,” *Science Robotics*, vol. 5, no. 47, p. eabc5986, 2020.

[49] H. Lai, W. Zhang, X. He, C. Yu, Z. Tian *et al.*, “Sim-to-real transfer for quadrupedal locomotion via terrain transformer,” in *IEEE International Conference on Robotics and Automation (ICRA)*, 2023, pp. 5141–5147.

[50] Y. Cheng, H. Liu, G. Pan, H. Liu, and L. Ye, “Quadruped robot traversing 3d complex environments with limited perception,” in *IEEE/RSJ International Conference on Intelligent Robots and Systems (IROS)*, 2024, pp. 9074–9081.

[51] F. Wu, X. Nal, J. Jang, W. Zhu, Z. Gu *et al.*, “Learn to teach: Sample-efficient privileged learning for humanoid locomotion over real-world uneven terrain,” *IEEE Robotics and Automation Letters*, vol. 10, no. 9, pp. 9048–9055, 2025.

[52] R. Seto, G. Li, K. Kutsuzawa, D. Owaki, and M. Hayashibe, “Two-stage learning of cpg and postural reflex toward quadruped locomotion on uneven terrain with simple reward,” *IEEE Access*, vol. 13, pp. 106 103–106 114, 2025.

[53] I. M. A. Nahrendra, B. Yu, and H. Myung, “Dreamwaq: Learning robust quadrupedal locomotion with implicit terrain imagination via deep reinforcement learning,” in *IEEE International Conference on Robotics and Automation (ICRA)*, 2023, pp. 5078–5084.

[54] S. Chen, Z. Wan, S. Yan, C. Zhang, W. Zhang *et al.*, “Slr: Learning quadruped locomotion without privileged information,” in *Conference on Robot Learning (CoRL)*, 2024.

[55] C. Mastalli, I. Havoutis, M. Focchi, D. Caldwell, and C. Semini, “Motion planning for quadrupedal locomotion: Coupled planning, terrain mapping, and whole-body control,” *IEEE Transactions on Robotics*, vol. 36, no. 6, pp. 1635–1648, 2020.

[56] T. Durdzik, M. Chignoli, G. Bledt, B. Lim, A. Miller *et al.*, “Robust autonomous navigation of a small-scale quadruped robot in real-world environments,” in *IEEE/RSJ International Conference on Intelligent Robots and Systems (IROS)*, 2020, pp. 3664–3671.

[57] D. Hoeller, L. Wellhausen, F. Farshidian, and M. Hutter, “Learning a state representation and navigation in cluttered and dynamic environments,” *IEEE Robotics and Automation Letters*, vol. 6, no. 3, pp. 5081–5088, 2021.

[58] Z. Xiong, J. Eappen, A. Qureshi, and S. Jagannathan, “Model-free neural lyapunov control for safe robot navigation,” in *IEEE/RSJ International Conference on Intelligent Robots and Systems (IROS)*, 2022, pp. 5572–5579.

[59] Q. Liao, Z. Li, A. Thirugnanam, J. Zeng, and K. Sreenath, “Walking in narrow spaces: Safety-critical locomotion control for quadrupedal robots with duality-based optimization,” in *IEEE/RSJ International Conference on Intelligent Robots and Systems (IROS)*, 2023, pp. 2723–2730.

[60] J. Kim, T. Li, and S. Ha, “Armp: Autoregressive motion planning for quadruped locomotion and navigation in complex indoor environments,” in *IEEE/RSJ International Conference on Intelligent Robots and Systems (IROS)*, 2023, pp. 2731–2737.

[61] S. Feng, Z. Zhou, J. Smith, M. Asselmeier, Y. Zhao, and P. Vela, “Gpf-bg: A hierarchical vision-based planning framework for safe quadrupedal navigation,” in *IEEE International Conference on Robotics and Automation (ICRA)*, 2023, pp. 1968–1975.

[62] M. Seo, R. Gupta, Y. Zhu, A. Skoutnev, L. Sentis, and Y. Zhu, “Learning to walk by steering: Perceptive quadrupedal locomotion in dynamic environments,” in *IEEE International Conference on Robotics and Automation (ICRA)*, 2023, pp. 5099–5105.

[63] U. Unlu, M. Gonçalves, D. Chaikalis, A. Tzes, and F. Khorrami, “A control barrier function-based motion planning scheme for a quadruped robot,” in *IEEE International Conference on Robotics and Automation (ICRA)*, 2024, pp. 12 172–12 178.

[64] S. Imai, M. Zhang, Y. Zhang, M. Kierebiński, R. Yang *et al.*, “Vision-guided quadrupedal locomotion in the wild with multi-modal delay randomization,” in *IEEE/RSJ International Conference on Intelligent Robots and Systems (IROS)*, 2022, pp. 5556–5563.

[65] N. Rudin, D. Hoeller, M. Bjelonic, and M. Hutter, “Advanced skills by learning locomotion and local navigation end-to-end,” in *IEEE/RSJ International Conference on Intelligent Robots and Systems (IROS)*, 2022, pp. 2497–2503.

[66] G. Bellegarda, M. Shafee, and A. Ijspeert, “Visual cpg-rl: Learning central pattern generators for visually-guided quadruped locomotion,” in *IEEE International Conference on Robotics and Automation (ICRA)*, 2024, pp. 1420–1427.

[67] H. Zhang, Z. Li, X. Zeng, L. Smith, K. Stachowicz *et al.*, “Traversability-aware legged navigation by learning from real-world visual data,” *arXiv preprint arXiv:2410.10621*, 2024.

[68] Z. Fu, A. Kumar, A. Agarwal, H. Qi, J. Malik, and D. Pathak, “Coupling vision and proprioception for navigation of legged robots,” in *IEEE/CVF Conference on Computer Vision and Pattern Recognition (CVPR)*, 2022, pp. 17 273–17 283.

[69] S. Katreer, N. Yokoyama, D. Batra, S. Ha, and J. Truong, “Vinl: Visual navigation and locomotion over obstacles,” in *IEEE International Conference on Robotics and Automation (ICRA)*, 2023, pp. 2018–2024.

[70] M. Mittal, C. Yu, Q. Yu, J. Liu, N. Rudin *et al.*, “Orbit: A unified simulation framework for interactive robot learning environments,” *IEEE Robotics and Automation Letters*, vol. 8, no. 6, pp. 3740–3747, 2023.

[71] L. Pinto, M. Andrychowicz, P. Welinder, W. Zaremba, and P. Abbeel, “Asymmetric actor critic for image-based robot learning,” in *Robotics: Science and Systems (RSS)*, 2018.

[72] J. Schulman, F. Wolski, P. Dhariwal, A. Radford, and O. Klimov, “Proximal policy optimization algorithms,” *arXiv preprint arXiv:1707.06347*, 2017.

[73] D. Kingma and M. Welling, “Auto-encoding variational bayes,” *arXiv preprint arXiv:1312.6114*, 2013.

[74] T. Haarnoja, A. Zhou, P. Abbeel, and S. Levine, “Soft actor-critic: Off-policy maximum entropy deep reinforcement learning with a stochastic actor,” in *International Conference on Machine Learning (ICML)*, 2018, pp. 1861–1870.